REVIEW

**ADVANCED
ELECTRONIC
MATERIALS**
Open Access

www.advelectronicmat.de

Raman Spectroscopy Application in Anisotropic 2D Materials

Xun Zhao, Zhipu Li, Shiru Wu, Min Lu,* Xiaoji Xie, Da Zhan, and Jiaxu Yan*

In recent years, anisotropic 2D materials (black phosphorus, ReS_2, WTe_2, etc.) have garnered significant attention due to their orientation-dependent physical and chemical properties, along with their potential applications in micro-nano device development, such as crystal-based diodes, polarized light photodetectors, and directional heat transfer. As a practical, quick, and nondestructive characterization tool, Raman spectroscopy, with its unique and unmatched advantages in studying anisotropic materials, plays a crucial role. It enables lattice orientation identification, investigation of structural phase transitions, and examination of anisotropic lattice vibrations, among other aspects. Here, a comprehensive review of recent developments in Raman spectroscopy research on anisotropic materials is provided. To begin, this study introduces the classification of anisotropic materials before delving into the polarized Raman spectroscopy principle. Various research directions of Raman spectroscopy in anisotropic materials are explored, including lattice orientation identification, temperature dependence, interlayer coupling, electron–phonon interaction, thickness dependence, and high-pressure phase transition. Finally, potential future directions in the field of Raman spectroscopy for anisotropic materials are discussed, and the potential challenges that may arise are addressed.

1. Introduction

The anisotropic 2D materials, typified by black phosphorus (BP), WTe_2, ReS_2, etc, have attracted extensive attention due to their exceptional optical, thermal, and electromagnetic properties.[1–9] 2D anisotropic materials offer the possibility of developing a new generation of multifunctional low-dimensional flexible electronic and optoelectronic devices, such as polarization-sensitive photodetectors,[10–16] ultrahigh photoresponsivity,[17–19] energy storage,[20,21] photocatalysis,[22–25] humidity sensors[26,27] etc. For instance, the hole Hall mobility of BP-based field-effect transistors (FETs) varies by 1.6-fold in the "zigzag" and "armchair" directions[9] Triclinic ReS_2 exhibits charge distributions primarily along the zigzag direction, leading to faster charge carrier diffusion and the strongest Raman enhancement when CuPc molecules align this way, offering insights into the chemical mechanism-based surface-enhanced Raman spectroscopy (SERS) enhancement and emphasizing the importance of substrate symmetry[28]

Raman spectroscopy has played a crucial role in characterizing 2D materials, allowing the determination of layer thickness[29] edge chirality[30] lattice orientation[31] doping,[32,33] alloy composition,[34] applied stress,[35–38] thermal effects,[39] structural phase transitions[40] defects,[7,41] and other properties. This nondestructive and rapid characterization tool has been instrumental in the advancement of 2D materials research, particularly for anisotropic materials. Raman spectroscopy facilitates a deep understanding of the properties of anisotropic materials in two dimensions, enabling further exploration of their applications. Additionally, it allows for in-depth studies of physical processes, such as electron–phonon coupling, in the Raman scattering process.[42]

The focus of this paper is to review the applications and characterization of Raman spectroscopy in 2D anisotropic materials, covering aspects like the classification and structure of anisotropic materials, the theory behind Raman spectroscopy, various Raman spectroscopy instrumentation, and the characterization of each material and its practical uses.

X. Zhao, Z. Li, S. Wu, M. Lu, X. Xie, J. Yan
Key Laboratory of Flexible Electronics (KLOFE) & Institute of Advanced Materials (IAM)
Nanjing Tech University (Nanjing Tech)
Nanjing 211816, P. R. China
E-mail: iammlv@njtech.edu.cn; yanjiaxu@ciomp.ac.cn
D. Zhan, J. Yan
Changchun Institute of Optics, Fine Mechanics & Physics (CIOMP)
Chinese Academy of Sciences
Changchun 130033, P. R. China
D. Zhan, J. Yan
University of Chinese Academy of Sciences
Chinese Academy of Sciences
Beijing 100049, P. R. China

**ADVANCED
SCIENCE NEWS**

www.advancedsciencenews.com

**ADVANCED
ELECTRONIC
MATERIALS**

www.advelectronicmat.de

Table 1. Classification of anisotropic 2D materials by their point symmetries.[46–56]

Symmetry	Materials	Tensor			
D_{2h}	BP[45], GeSe[47], PdSe$_2$[48], GeAs$_2$[49], ZrTe$_5$[50]	$A_g\begin{pmatrix}a&0&0\\0&b&0\\0&0&c\end{pmatrix}$	$B1g\begin{pmatrix}0&d&0\\d&0&0\\0&0&0\end{pmatrix}$	$B2g\begin{pmatrix}0&0&e\\0&0&0\\e&0&0\end{pmatrix}$	$B3g\begin{pmatrix}0&0&0\\0&0&f\\0&f&0\end{pmatrix}$
C_{2h}	MoTe$_2$(T'phase)[46], Ta$_2$NiS$_5$, GaTe[51], TiS$_3$[52], GeP[53]	$A_g\begin{pmatrix}a&d&0\\d&b&0\\0&0&c\end{pmatrix}$	$B_g\begin{pmatrix}0&0&e\\0&0&f\\e&f&0\end{pmatrix}$		
C_i	ReS$_2$/ReSe$_2$[54]	$A_g\begin{pmatrix}a&d&e\\d&b&f\\e&f&c\end{pmatrix}$			
C_{2v}	MoTe$_2$(Td phase)[46], WTe$_2$[55]	$A_1(z)\begin{pmatrix}a&0&0\\0&b&0\\0&0&c\end{pmatrix}$	$A2\begin{pmatrix}0&d&0\\d&0&0\\0&0&0\end{pmatrix}$	$B1(x)\begin{pmatrix}0&0&e\\0&0&0\\e&0&0\end{pmatrix}$	$B2(y)\begin{pmatrix}0&0&0\\0&0&f\\0&f&0\end{pmatrix}$

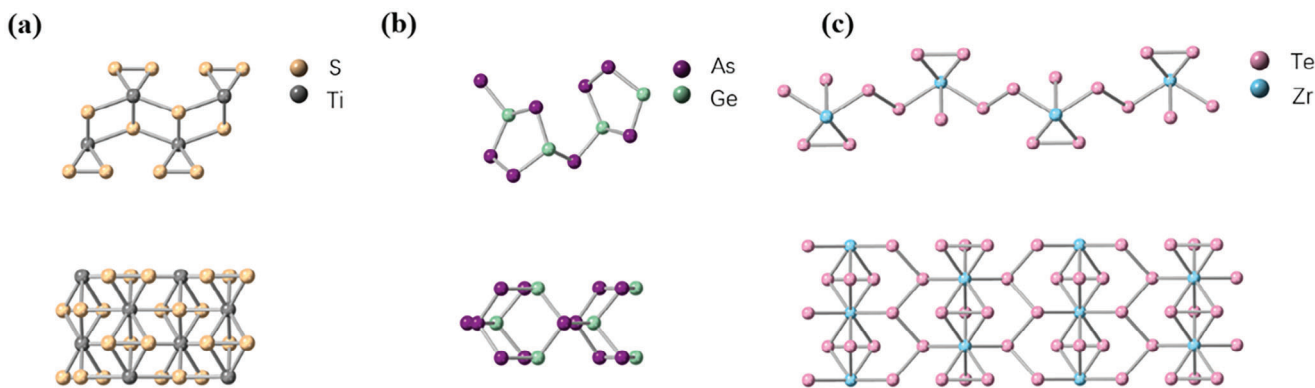## 2. Anisotropic 2D Materials and Their Classification

Over the past decade, 2D materials have been at the forefront of research, which typically form strong in-plane chemical bonds while exhibiting weak van der Waals bonds out-of-plane. They display diverse symmetries such as D_{6h} (found in graphene, MoS(Se)$_2$, WS(Se)$_2$, GaSe(S), h-BN, etc.), D_{3d} (in SnSe$_2$, and Bi2Te(Se)$_3$), D_{2h} (in black phosphorus (BP), GeS(Se), SnS(Se)), C_{2h} (in GaTe), and C_i (in ReS(Se)$_2$).[43,44] Notably, 2D materials with lower symmetries like D_{2h}, C_{2h}, and C_i exhibit in-plane anisotropy. This anisotropy introduces an additional degree of freedom compared to isotropic materials, leading to diverse physical properties.

Common 2D materials like graphene, hBN, and MoS$_2$, which have symmetrical lattices, offer consistent isotropic in-plane properties, beneficial for many electronic and photonic applications. In contrast, 2D materials with anisotropy, where properties differ based on spatial orientation, provide additional tailoring possibilities and potential for multifunctional nanodevices. Point symmetry, vital in determining anisotropy, affects Raman modes and their activity. We briefly discuss the point symmetries in anisotropic 2D materials and their associated Raman tensors in **Table 1**, noting that external factors and structural variations can influence these symmetries. Some 2D materials can even achieve orthorhombic symmetry under specific conditions or through structural engineering.

The orthorhombic crystal family encompasses the C_{2v} and D_{2h} point groups. The completely symmetric representations A, A$_1$, or A$_g$ have diagonal Raman tensors with distinct diagonal elements. Crystals in the C_{2h} point group, which are monoclinic, possess two Raman tensors for modes with distinct symmetries. The Raman tensor for the fully symmetric representations (A, A$_1$, A$_g$) in the C_{2h} group isn't diagonal due to a nonzero xz element.[45] For MoTe$_2$, distinct phases exhibit varied point symmetries. The 1T' and Td phase structures only differ in their interlayer stacking. The 1T' phase, being monoclinic, has a stacking angle of ≈93.9° and includes symmetry elements like a twofold screw axis (C_{2x}), a horizontal mirror plane (M_x), and an inversion center, placing it in the C_{2h} point group. Conversely, the orthorhombic-stacked Td phase possesses a twofold screw axis (C_{2z}), a diagonal glide plane (M_y), and a vertical mirror plane (M_x), aligning it with the C_{2v} group.[46] Lastly, the triclinic crystal family consists of the C_i point groups, characterized by the sole nontrivial symmetry operation of an inversion center. Raman-active modes in the C_i groups belong to the Ag representation,[45] where all Raman tensor elements are nonzero, as presented in Table 1.
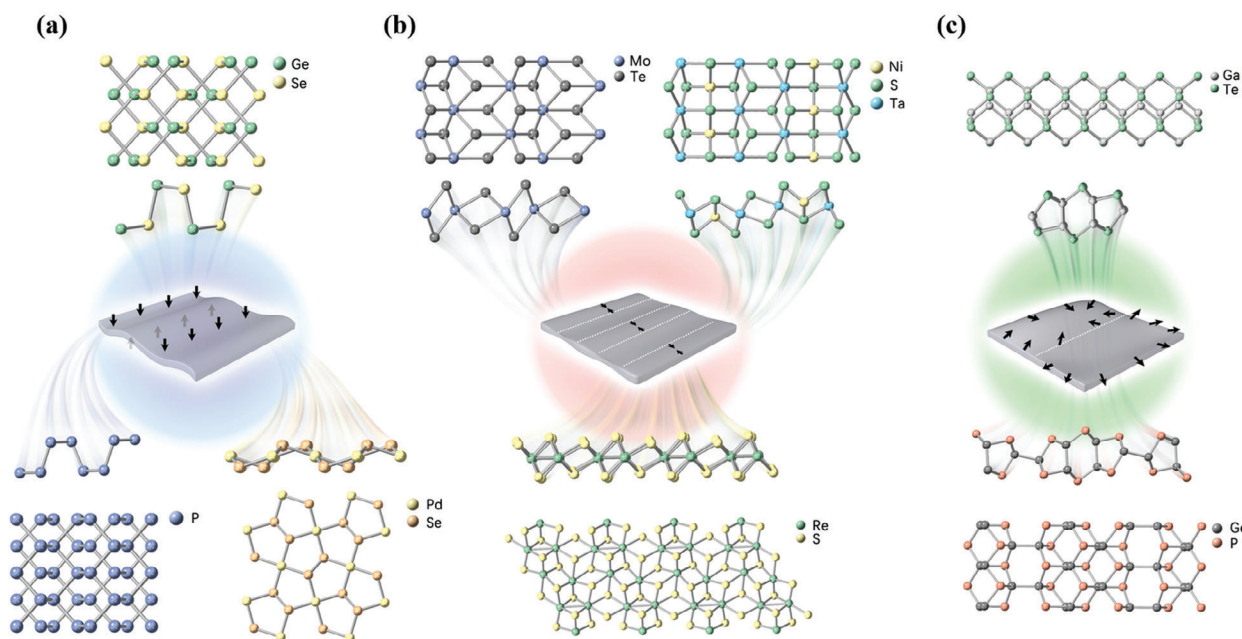
Figure 1. Regularly shaped anisotropic 2D materials resulting from different force patterns of three 2D materials. a) The wave-fold type. b) The rhombic type. c) The polygonal type.

**ADVANCED
SCIENCE NEWS**

www.advancedsciencenews.com

**ADVANCED
ELECTRONIC
MATERIALS**

www.advelectronicmat.de

Figure 2. Irregularly shaped anisotropic 2D materials a) TiS$_3$ side and top views are shown, followed by b) side and top views of GeAs$_2$, and finally c) side and top views of ZrTe$_5$ are presented.
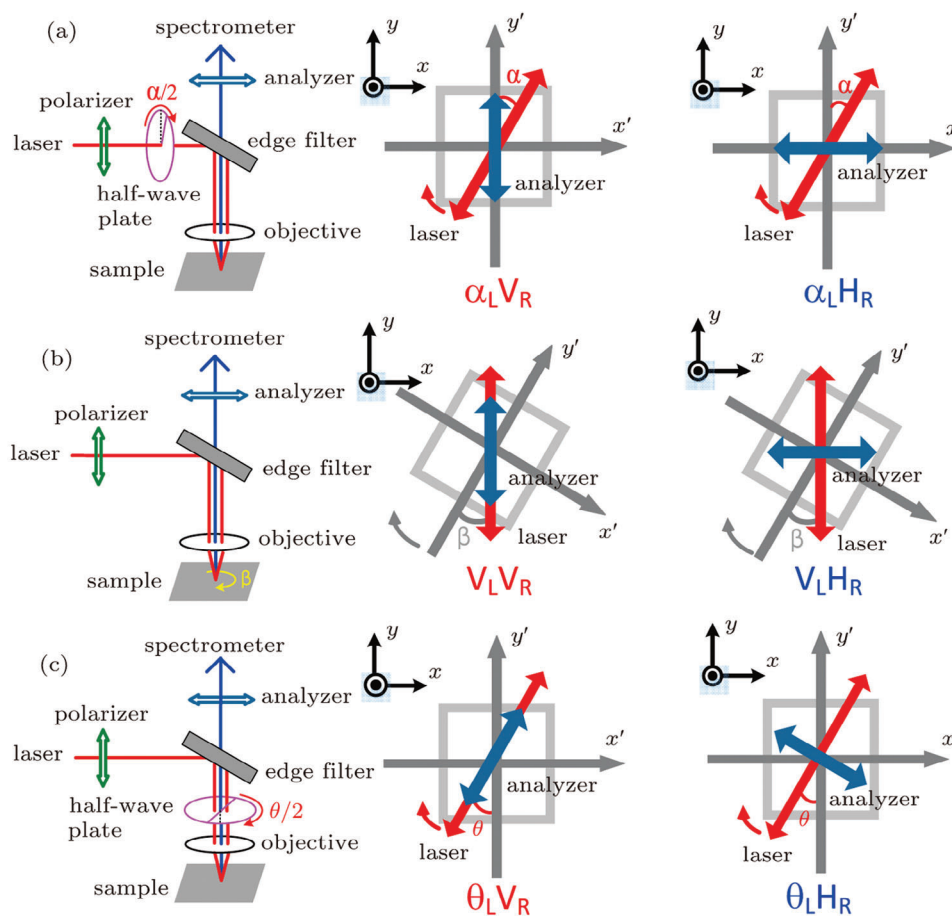
2.1. Anisotropic 2D Materials with Regular Shapes

While the point group classification offers a rigorous mathematical structure grounded in crystallography, we can also categorize anisotropic 2D materials into subclasses based on shared structural characteristics rather than their underlying symmetries. As shown in **Figure 1**, the traditional side-view shapes of anisotropic 2D materials can be primarily categorized into wave-fold, rhombus, and polygon types. The varied forms of anisotropic 2D materials-be it wave-fold, rhombus, or polygon-can be interpreted as manifestations of fictitious in-plane stresses acting on the lattice structure, leading to anisotropic contraction or expansion within the lattice. For example, a wave-fold can be visualized as the material's response to alternating compressions and expansions in the vertical plane. The rhombic form arises from alternating in-plane uniaxial tensile and compressive stresses. For a polygonal structure, the in-plane stresses are more complex. Adjacent regions within the material alternate between tension and compression.

Black phosphorus stands out as one of the most remarkable 2D layered semiconductors in the next generation of optoelectronics and excellent qualities, including strong carrier mobility and a directly controllable band gap energy, electrical, thermal properties and excellent anisotropic optical.[57–59] Figure 1a illustrates the graphene-like orthorhombic crystal structure of black phosphorus, where phosphorus atoms form a honeycomb lattice. Unlike graphene and other 2D atomically planar nanomaterials, BP consists of folded bilayers. In the BP monolayer, each P atom forms covalent bonds with three neighboring P atoms using a pair of unshared electrons (with a bond length of 2.18 Å), creating
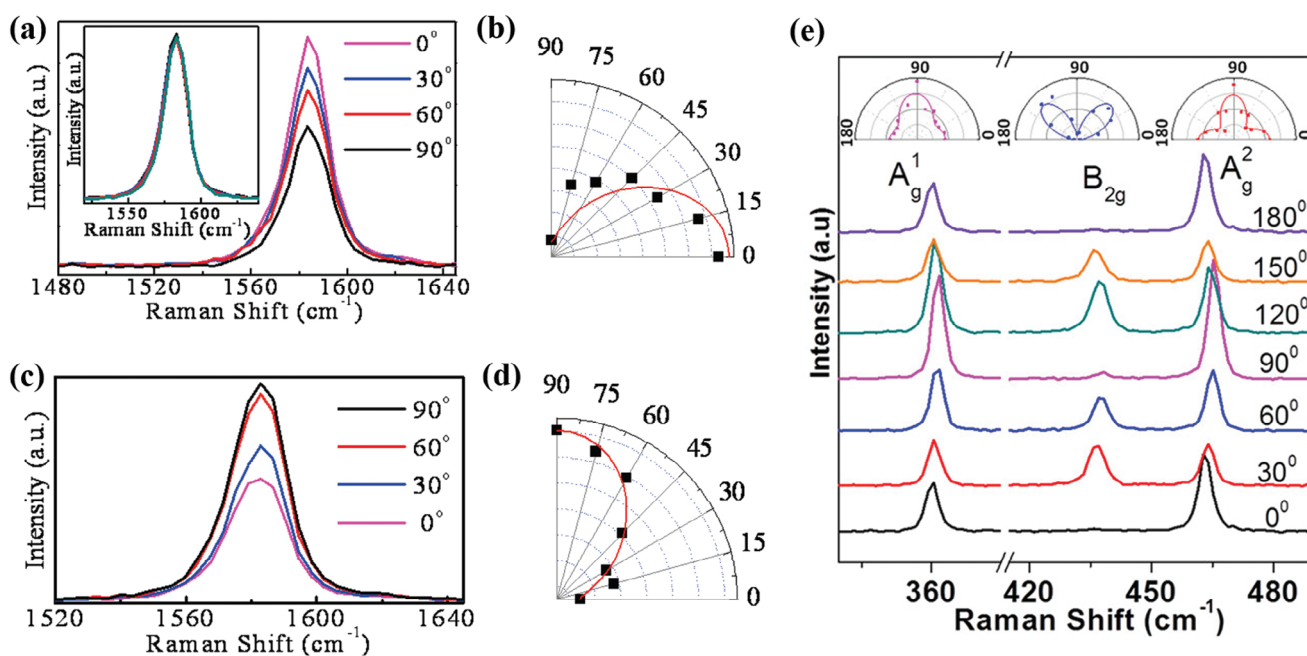
Figure 3. a–d) Raman spectra of graphene at different polarization angles.[80] Typical Raman spectra for incident laser with polarization angles 0°, 30°, 60°, and 90° with respect to the armchair (a) or zigzag edges (c). Reproduced with permission.[80] Copyright 2010, American Chemical Society. e) Raman spectra of BP at different polarization angles. Reproduced with permission.[81] Copyright 2016, American Chemical Society.

**ADVANCED
SCIENCE NEWS**

www.advancedsciencenews.com

**ADVANCED
ELECTRONIC
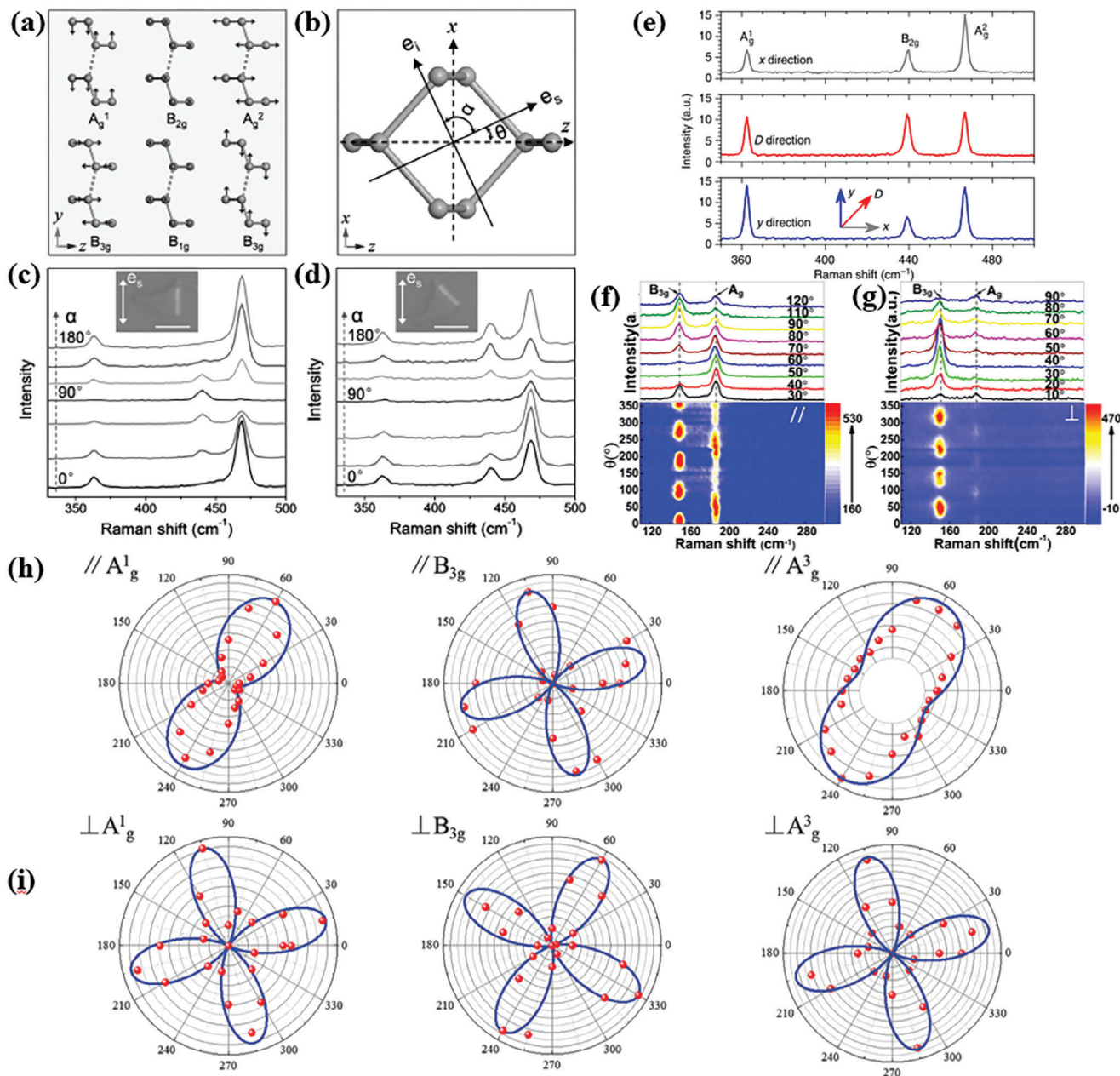MATERIALS**

www.advelectronicmat.de

Figure 4. The following schematic diagrams illustrate three typical configurations used in angle-resolved polarised Raman spectroscopy: a) $\alpha_L V_R$ and $\alpha_L H_R$, b) $V_L V_R$ and $V_L H_R$, c) $\theta_L V_R$ and $\theta_L H_R$ Reproduced with permission.[82] Copyright 2017, IOP Publishing.

a wave-like structure. Among these three adjacent phosphorus atoms, two lie on the same plane at an angle of 98.15°, while the third P atom deviates at an angle of 103° between the two layers. This unique arrangement leads to a variety of anisotropic physical properties, encompassing optics, mechanics, thermoelectricity, and electrical conductivity. The subsequent layers are stacked in an ABA stacking order along the z-direction, held together by weak van der Waals interactions. This layered structure allows for the extraction of single or multiple BP films from bulk crystals using mechanical or liquid exfoliation techniques, with an interlayer spacing of ≈5 Å.

Layered group IV monochalcogenides, including SnSe, SnS, GeSe, and GeS, exhibit a wave-like structure similar to that of BP. However, compared to the single elements in BP, group IV monochalcogenides compounds consist of two elements with distinct electronegativity, leading to broken inversion symmetry in the odd-even layer and resulting in poorer symmetry and more diverse physical properties. Previous studies have shown that these 2D materials possess semiconductor properties, with bandgap energy covering some of the infrared and visible light ranges. The phosphorus like wire structure also exhibits anisotropic conductivity and thermal conductivity, exhibiting high thermoelectric performance and ultra-low thermal conductivity. Theoretical studies suggest that 2D group

IV monochalcogenides will display significant piezoelectricity and strong ferroelectricity, distinguishing them from conventional 2D anisotropic materials within the plane. Among them, 2D GeSe exhibits excellent stability in air and high in-plane anisotropy. Classified as a p-type semiconductor, GeSe features band gaps ranging from 1.1 to 1.2 eV, both direct and indirect, effectively aligning with the solar spectrum and making it suitable for solar applications. Moreover, GeSe demonstrates a visible absorption coefficient of ≈105 cm^{-1} and remarkable hole mobility of up to 1.6 cm2 V^{-1} s^{-1}. Comprising four Pd and eight Se atoms in an orthogonal lattice unit cell, a single layer of $PdSe_2$ is held together mainly by van der Waals forces. From a side perspective, $PdSe_2$ appears as a five-sided circular structure with a wavy folded pattern, reminiscent of black phosphorus. Unlike BP, $PdSe_2$ exhibits air stability and can be fabricated through chemical vapor deposition,[40] positioning it as a promising candidate for practical electronic applications.[7,41–61] Overall, these findings suggest that the utilization of 2D pentagonal materials could foster the development of pioneering electronic devices, capitalizing on charge coupling, spin, and additional degrees of freedom arising from subtle asymmetry. 2D rhombic anisotropic materials are characterized by their rhombic shape in the lateral view and mainly consist of $1T_d$ WTe_2, 1T"$MoTe_2$, ReS_2, and $ReSe_2$, in contrast to the common hexagonal (2H) phase crystalline TMDs

ADVANCED
SCIENCE NEWS

www.advancedsciencenews.com

ADVANCED
ELECTRONIC
MATERIALS
Open Access

www.advelectronicmat.de

Figure 5. a) In the case of BP, atomic displacements are examined for Raman-active modes b) Raman spectra of the BP sample were obtained under different polarisation angles α in the polarized Raman experiments ($\alpha = 0°-180°$).[85] The OM images are provided as insets in (c,d),[85] with a scale bar of 5 μm. Reproduced with permission.[85] Copyright 2015, John Wiley and Sons. e) The Raman scattering resolved by polarization is investigated in this study.[86] The Raman spectra of a thin film composed of BP layers are analyzed by utilizing a 532 nm laser with linear polarization. The incident laser is polarized in the z-axis direction. The resulting Raman spectra exhibit distinct features when the excitation laser's polarization is aligned along the x-axis (represented by the color gray), D-axis (represented by the color red), and y-axis (represented by the color blue). Reproduced with permission.[86] Copyright 2017, American Chemical Society. Angle-resolved Raman spectra and corresponding contour color map of GeSe nanoflakes measured in the f) parallel and g) cross-polarization configurations.[88] Reproduced with permission.[88] Copyright 2017, American Chemical Society. h) Angle-resolved Raman scattering intensities of A^1_g, B_{3g}, and A^3_g modes under parallel configuration.[91] i) Angle-resolved Raman scattering intensities of A^1_g, B_{3g}, and A^3_g modes under cross configuration.[91] Reproduced with permission.[91] Copyright 2018, Wiley-VCH.

like MoS_2 and WSe_2. Among these, $1T_d$ WTe_2 and $1T''$ $MoTe_2$ are semi-metallic type II Weyl candidates, holding potential for spintronics applications. On the other hand, ReS_2 and $ReSe_2$ are semiconductors with moderate band gaps, making them suitable for optoelectronic materials. Figure 1b illustrates the atom-

istic bead and stick structures of the 1T' phases of $MoTe_2$, where the Te atoms are staggered with coordination distortion. The 1T' phase exhibits a semimetallic property with an extended in-plane lattice constant. The distorted 1T phase of WTe_2 remains stable, leading to in-plane anisotropy in various material prop-
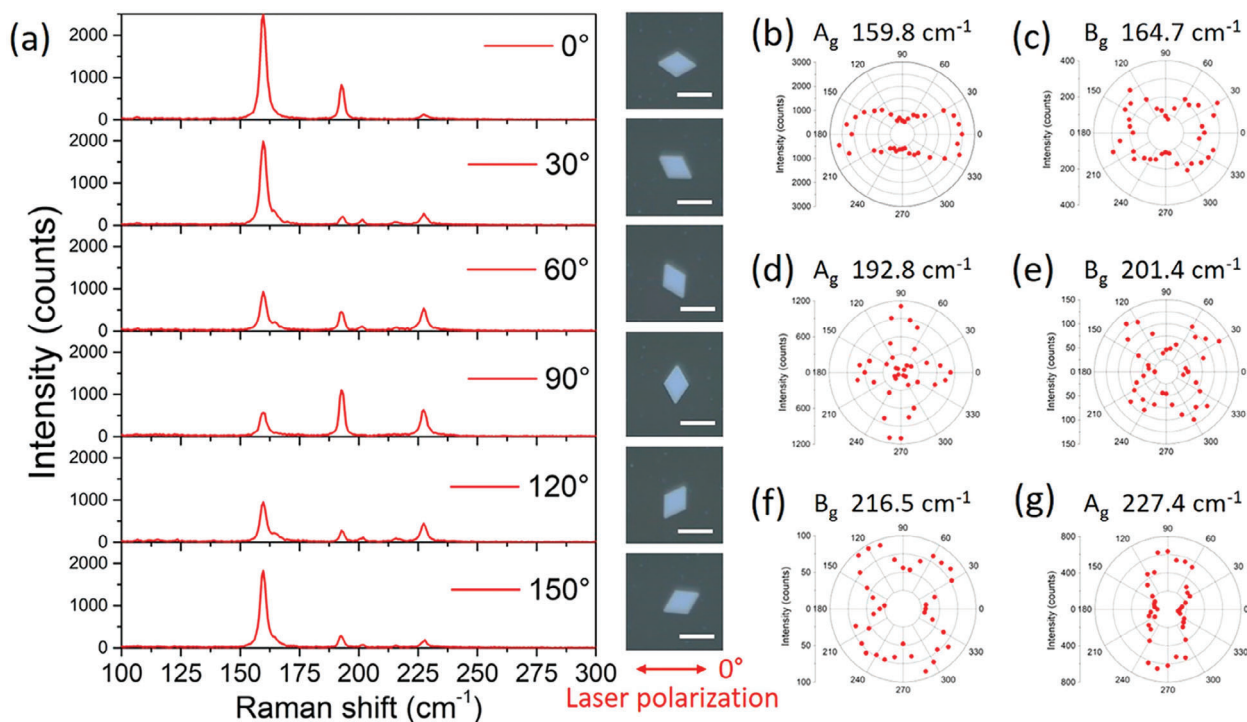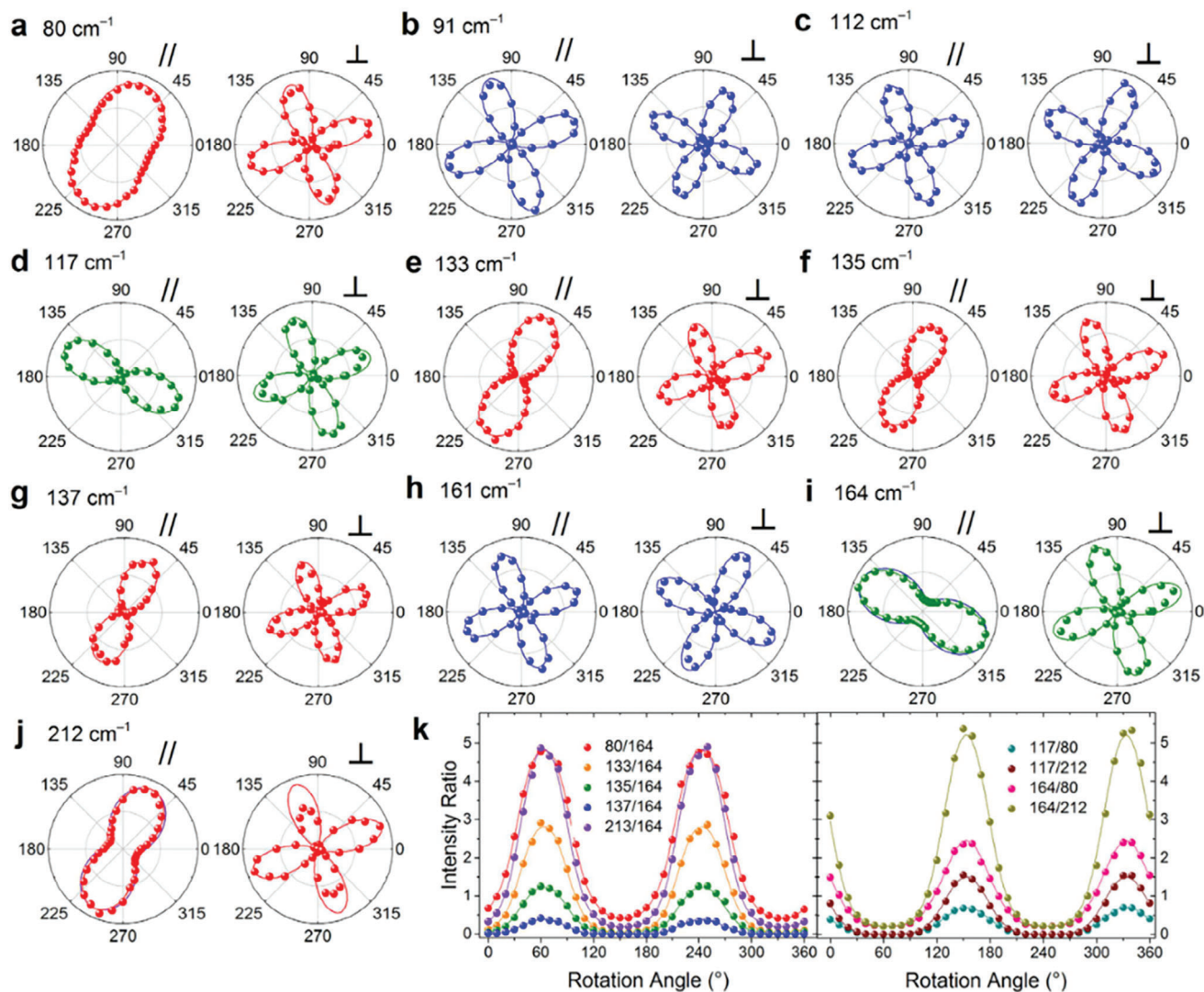
Figure 6. Polarization Raman spectra of M-PdSe$_2$ excited by a 532 nm laser. a) Raman spectra were acquired for M-PdSe$_2$ grown on c-plane sapphire using the $z(xx)\bar{z}$ polarization setup. The crystal orientation was varied from 0° to 150° with respect to the laser polarization direction. b–g) Polar plots were generated experimentally by plotting the intensity peaks against the crystal rotation angle relative to the polarization of the laser. Reproduced with permission.[92] Copyright 2022, American Chemical Society.
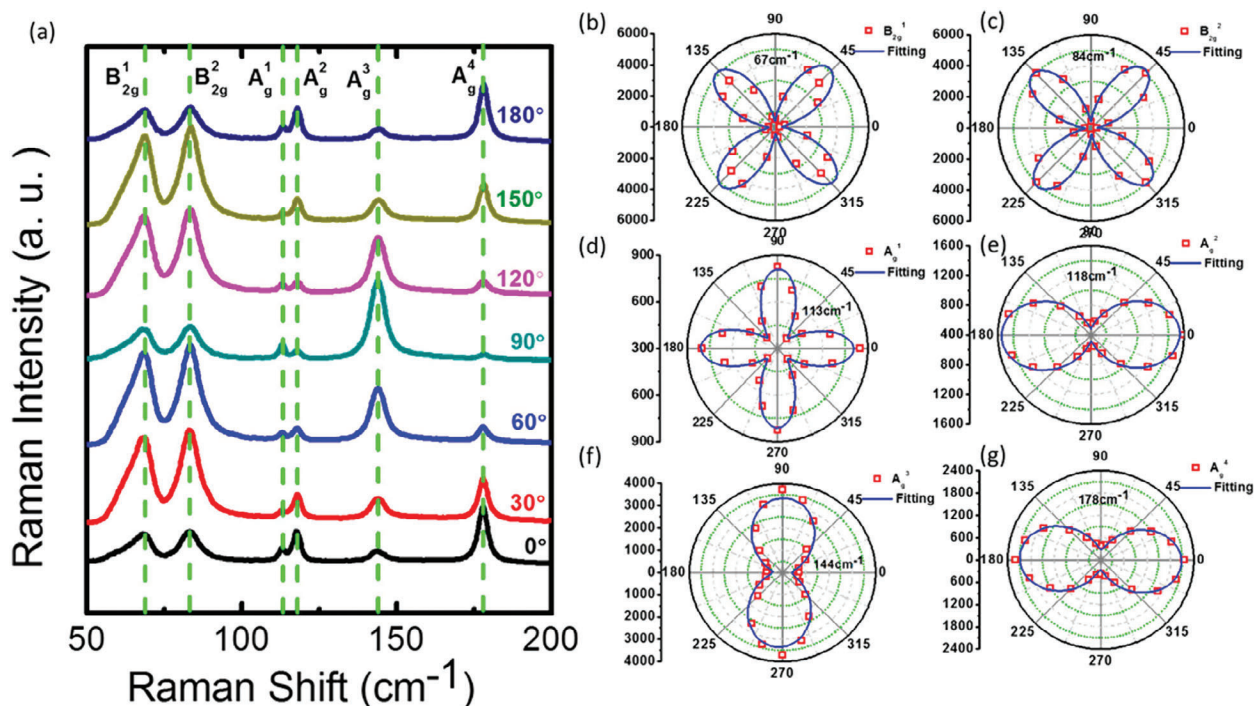
Figure 7. a) Raman spectra of a freshly exfoliated flake as a function of the angle of rotation between the flake and the incident polarization.[93] b–g) correspond to B_{2g}^1, B_{2g}^2, A_g^1, A_g^2, A_g^3, and A_g^4 Raman modes which are located at 67, 84, 113, 118, 144, and 178 cm^{-1} Reproduced with permission.[93] Copyright 2016, American Chemical Society.

**ADVANCED
SCIENCE NEWS**

www.advancedsciencenews.com

**ADVANCED
ELECTRONIC
MATERIALS**

www.advelectronicmat.de

Figure 8. The Raman intensities were detected for ten modes, and their angular dependence is examined in Song's study. Reproduced with permission.[94] Copyright 2016, Springer Nature.

erties, which has generated significant attention due to its remarkable magnetoresistance[62,64] and impressive thermoelectric properties.[64,65] Similarly, rhenium disulfide ReS_2 has gained attention due to its anisotropic physical features and environmental stability.[67] The anisotropy arises from the distorted 1T crystal structure, forming a rhombic Re_4 structure due to the Peierls jump. The band gap of ReS_2 shows less reliance on the number of layers, contributing to higher charge carrier mobility along the orientation parallel to the Re chain (b-axis) and lower mobility along the a-axis. Additionally, Ta_2NiS_5, a compound of metal sulphones, belongs to the group of 2D in-plane anisotropic materials. Unlike extensively studied systems such as BP, SnSe, ReS_2, and TiS_3, which consist of one or two constituents, Ta_2NiS_5 comprises three elements, offering more opportunities for adjusting its physical properties through stoichiometric modifications. Its laminar van der Waals structure exhibits a tetrahedral arrangement of Ni atom sheets and an octahedral arrangement of Ta atom sheets, leading to significant anisotropic properties along

the a- and c- axes. When viewed from the side, Ta_2NiS_5 displays a rhombus shape, similar to the aforementioned 2D materials.

As shown in Figure 1c, we have explored two representative anisotropic materials in 2D: GaTe and GeP. These materials are classified as anisotropic 2D materials with polygonal structures due to their polygonal side view. Layered gallium telluride (GaTe) has garnered significant interest recently due to its exceptional photoresponsivity, response time, and thermoelectric characteristics. As a p-type semiconductor, GaTe has a direct bandgap of ≈1.65eV.[67,68] GaTe exhibits in-plane anisotropy and lacks strong symmetry, distinguishing it from commonly used 2D materials. It belongs to the C_{2h}^3 space group, which further sets it apart. van der Waals forces cause adjacent GaTe layers to stack on top of each other in the z-direction. In its bulk form, GaTe exhibits C_{2h}^3 (C2/m) symmetry with a twofold rotational axis C2 (y-axis) and a mirror plane σh (x−z plane). Recently, theoretical work by Jing et al. on 2D GeP_3 has been reported, showing that it exhibits higher chemical stability compared to BP, a moderate tunable
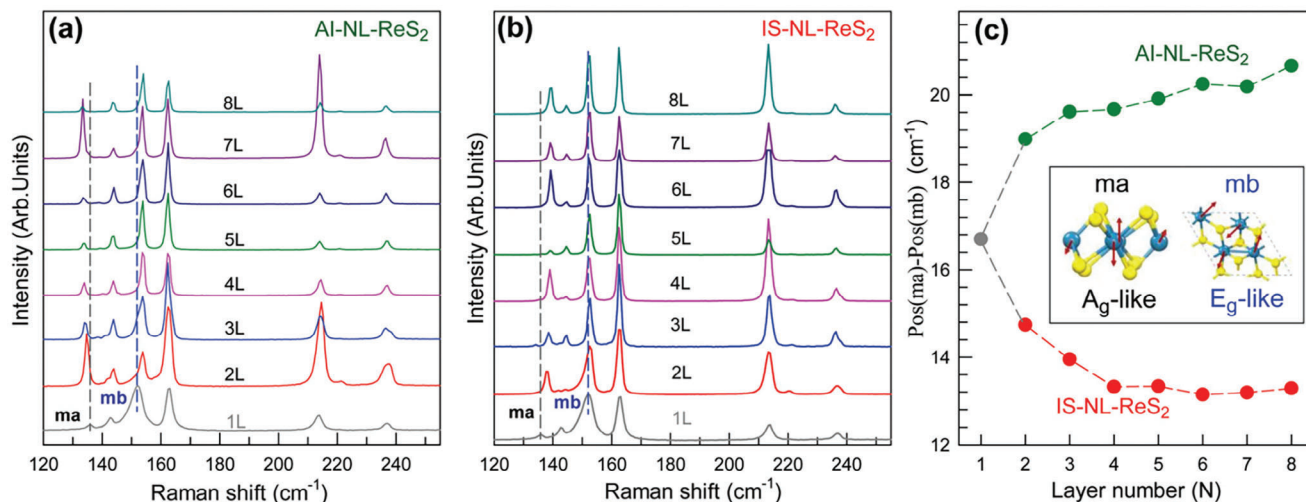
Figure 9. (a,b) Raman spectra of a) AI-stacked and b) IS-stacked 2–8L ReS$_2$ in the range of 120–250 cm^{-1}, together with that of 1L ReS$_2$ for comparison. The dashed lines are guides to the eye. c) Pos(mb)–Pos(ma) as a function of N for AI-stacked (green circles) and IS-stacked (red circles) 2–8L ReS$_2$. The inset shows the atom displacement of the modes ma and mb, which are indicated in (a,b). Reproduced with permission.[97] Copyright, 2016 Royal Society of Chemistry.

band gap ranging from 0 to 0.55 eV, and high mobility of up to 8.84×10^3 cm^2 V^{-1} s^{-1}. Additionally, the introduction of GeP into a Group IV compound, into the rapidly expanding 2D family, has demonstrated remarkable anisotropic physical features including mechanical, electronic, and transport properties both experimentally and theoretically.[70]

2.2. Irregularly Shaped Anisotropic 2D Materials

In this part, we will introduce three 2D materials categorized as 2D irregularly shaped anisotropic materials due to their irregular geometric shape in the side view. The monoclinic crystal structure of bulk TiS$_3$ (space group $p21m$) consists of stacked parallel
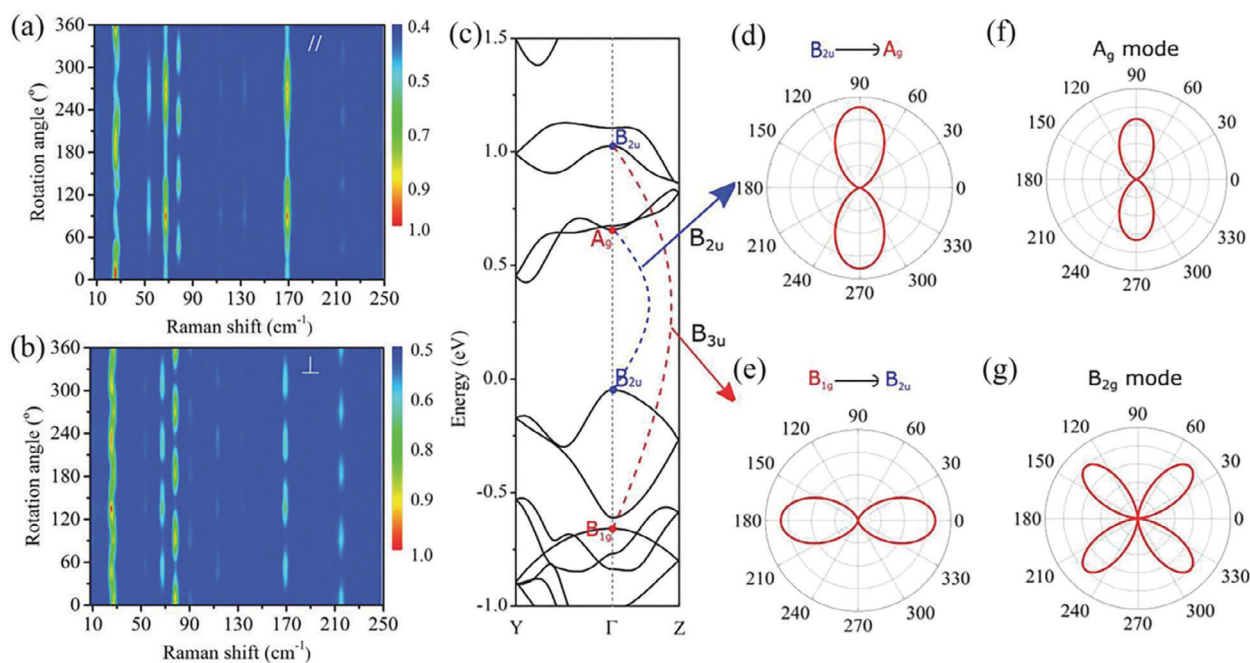
Figure 10. Normalized polarized Raman intensities for a 46.4 nm thick GeAs$_2$ flake are presented in (a,b), representing the parallel and perpendicular polarization configurations, respectively. To examine the absorption intensity and Raman intensity in bulk GeAs$_2$, two symmetry-permissible optical transitions are shown in (c–g).[99] The bulk GeAs$_2$ band structure is depicted along the Γ-Y and Γ-Z directions, where the Γ point is represented by red and blue solid points indicating irreducible representations (A$_g$, B$_{1g}$, and B$_{2u}$) of certain bands. The two potential optical transitions in bulk GeAs$_2$ and their corresponding symmetries in (d,e). Furthermore, f,g provide a schematic diagram of the Raman intensity for the A$_g$ and B$_{2g}$ modes. Reproduced with permission.[99] Copyright, 2018 John Wiley and Sons.
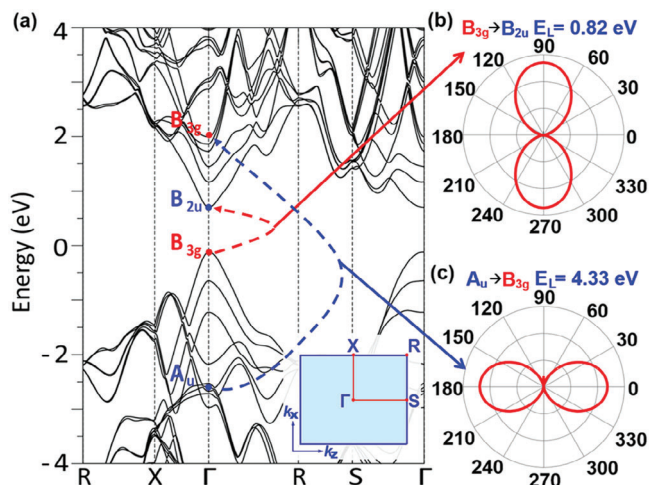
Figure 11. Optical selection rules in black phosphorus and the calculated anisotropic absorption. a) Calculated electronic band structure E(k) of tri-layer BP. B_{3g} bands are indicated by red labels, while B_{2u} and Au bands are indicated by blue labels at the Γ point. Inset: 2D Brillouin zone of tri-layer BP. (b,c) Calculated polarization dependence of the optical transition probability b) from B_{3g} to B_{2u} and c) from A_u to B_{3g} as indicated in panel a. Reproduced with permission.[81] Copyright 2016, American Chemical Society.

sheets, each comprising 1D chains of triangular TiS_3 units, held together by van der Waals forces (see **Figure 2a**). TiS_3 possesses lower cleavage energy than graphite, suggesting easy exfoliation for TiS_3.[71] Moreover, optical absorption measurements indicate that the bulk TiS_3 exhibits an optical gap of ≈1 eV.[72] TiS_3 has a wide range of applications in optoelectronic devices,[72–75] replacing graphene, MoS_2 and other 2D materials.

The 2D anisotropic in-plane family includes a new member, $GeAs_2$, which was studied by Li et al. showing significant frequency shifts with increasing thickness in layer-dependent phonon vibration. A polarization-sensitive photodetector was demonstrated using few-layer flakes of $GeAs_2$, achieving a dichroic ratio of ≈2. $GeAs_2$ exhibits distinctive vibrational behavior and inherent anisotropy, making it promising for investigating interlayer coupling and developing new electrical and optoelectronic devices.[77] Meanwhile, the extremely low thermal conductivity of $GeAs_2$ makes it a very promising candidate for thermoelectric applications.[50] Bulk $GeAs_2$, a member of the *Pbam* space group,[78] possesses orthorhombic structures (see Figure 2b).
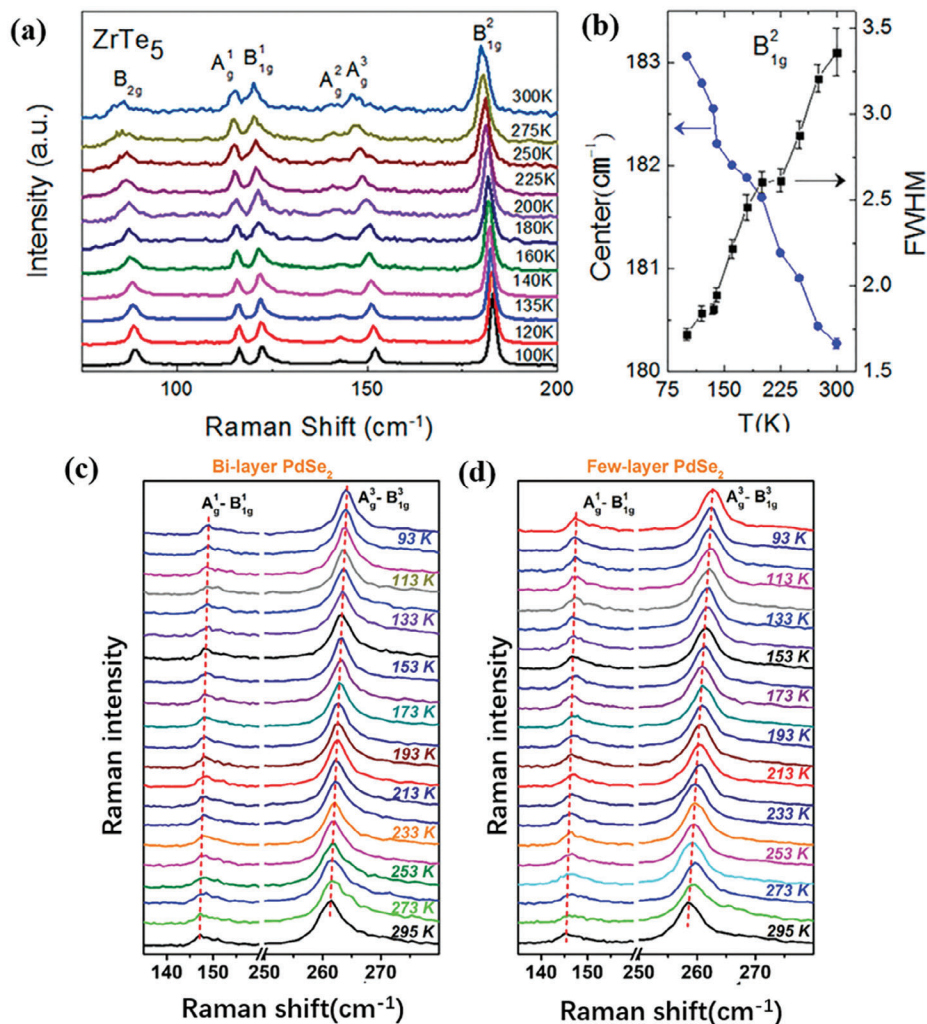
Furthermore, Qiu et al. conducted an extensive investigation into the anisotropy of few-layer $ZrTe_5$, including its optical and electrical properties. $ZrTe_5$'s high anisotropy arises from its unique atomic structure, evident in TEM images of its quasi-1D structure. The side and top views of the $ZrTe_5$ lattice structure are depicted in Figure 2c. $ZrTe_5$'s asymmetrical configuration when viewed laterally resembles the structure described earlier for the two aforementioned materials. Meanwhile, a systematic magnetic transport study of high-quality $ZrTe_5$ single crystals was carried out by Zhou et al. Clear quantum oscillations were observed at low temperatures, revealing the presence of nontrivial bands with tiny effective masses in $ZrTe_5$.[79]

3. The Principles of Raman Spectroscopy

When light interacts with a medium, three possible outcomes can occur: some of the light is absorbed, some is transmitted, and the rest is scattered. In most cases, the majority of light is transmitted, and only a small portion is scattered in all directions from the sample. If the medium is inhomogeneous and this inhomogeneity remains constant over time, the scattered light will have the same frequency as the incident light. This phenomenon is known as elastic scattering or Rayleigh scattering, and it is responsible for the blue appearance of the sky. On the other hand, if the inhomogeneity of the medium changes over time, the frequency of the scattered light will differ from that of the incident light. This type of scattering is called inelastic scattering and includes Raman scattering and Brillouin scattering, scattering below the incident light frequency is called Stokes scattering, scattering above the incident light frequency is called anti-Stokes scattering, and Stokes scattering and anti-Stokes scattering are collectively called Raman scattering. The Raman spectrum is obtained from the analysis of the intensity of the Raman scattered light as a function of the frequency shift relative to the incident light. Different types of Raman spectra exist, including resonance Raman spectra, surface-enhanced Raman spectroscopy, plasmon-enhanced Raman spectroscopy, and surface enhancement of Raman scattering, each providing unique information about the system. By analyzing Raman frequencies, peak positions, peak widths, and peak intensities, the spatial arrangement and interactions of atoms can be revealed, allowing for sample identification **Figure 3**.

As shown in **Figure 4a–e**, we juxtapose the Raman spectra of two representative 2D materials: isotropic graphene[79] and anisotropic BP.[81] For graphene, Raman peaks remain unshifted at 0°, 30°, 60°, and 90° polarization angles. In contrast, BP's Raman peaks noticeably shift with changing polarization angles. Notably, new Raman peaks emerge at 30° and 60°.

Raman spectroscopy offers a straightforward yet effective method for distinguishing between anisotropic and isotropic 2D materials. For certain specific situations with anisotropic 2D materials, standard Raman spectroscopy might not suffice. In these cases, polarization Raman spectroscopy is employed for more detailed investigation. Experimentally, researchers typically utilize three different configurations, with the prevalent setup being the fixed polarization directions of both incident and scattered lights along the primary axes (*x, y, z*).[81,82] The fundamental configuration, depicted in Figure 4a, rotates the incident laser's polarization by α degrees using a half-wave plate, set at α/2 degrees relative to its fast axis, while keeping the analyzer fixed. The sample remains aligned with lab coordinates. This method is favored for its efficiency and simplicity. Figure 4b shows a setup where the laser polarization is aligned along the *y*-axis using a polarizer. The analyzer's setting can be either on the *x* or *y*-axis, indicating cross or parallel polarization respectively. Acquiring accurate laser alignment with the sample can be challenging in this setup, adding complexity. Figure 4c illustrates an alternate to 4(b) but with a varied geometry, employing a half-wave plate between the edge filter and the objective lens while keeping the sample static. These configurations ensure meticulous control over polarization angles, crucial for studies on crystal directionality and phonon anisotropy.

**ADVANCED
SCIENCE NEWS**

www.advancedsciencenews.com

**ADVANCED
ELECTRONIC
MATERIALS**

www.advelectronicmat.de

Figure 12. a) The Raman spectroscopy of nanostructured $ZrTe_5$ crystals is presented, demonstrating its temperature dependence, b) The variations in peak positions and full width at half maximum of nanostructured $ZrTe_5$ crystals with temperature are shown. Reproduced with permission.[100] Copyright 2016, American Chemical Society. c,d) Temperature-dependent Raman spectra are provided for bi-layer and few-layer $PdSe_2$. Reproduced with permission.[101] Copyright 2021, Royal Society of Chemistry.

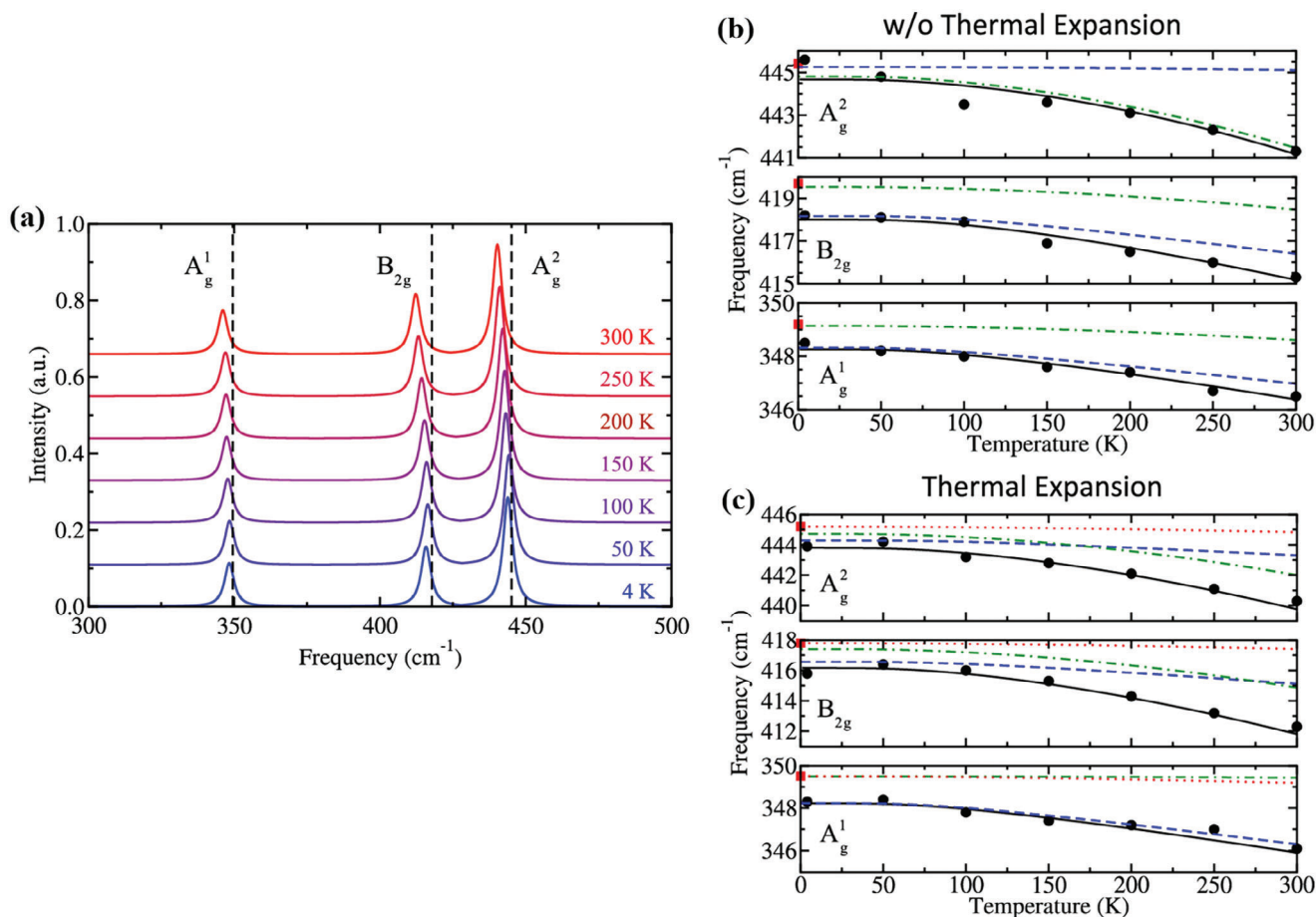## 4. Applications of Raman Spectroscopy to Anisotropic 2D Materials

In this chapter, we outline the applications of Raman spectroscopy in anisotropic 2D materials, discussing them under five key aspects.

4.1. Orientation Identification

In anisotropic 2D materials, lattice orientation influences the polarization of scattered light. Vibration patterns within the crystal vary in response to incident polarized light depending on the lattice orientation. Thus, assessing scattered light across different polarization states reveals details about the lattice orientation. This chapter delves into the impact of lattice orientation in various anisotropic 2D materials on Raman spectroscopy.

In previous work by Kim et al., it was found that Raman spectroscopy can determine the lattice orientation of BP[84] and has been used to reveal the crystalline orientation of black phosphorus (BP), where Raman intensity depends not only on the polarization angle "a" but also on the sample's rotation angle "q".[85] Among the six Raman active modes (depicted in **Figure** 5a–d, only the A_g^1, B_{2g}, and A_g^2 modes are observable when the incident laser is perpendicular to the sample plane, in accordance with the symmetry selection rule. The Raman scattering results of the x-, D-, and γ-direction polarization of BP are presented in Figure 5e.[86] Here the direction of D is 45° to both the x and γ directions within the x-γ plane. In this study, three Raman peaks are observed in thin-film BP regardless of polarization. These peaks occur at ≈470 cm^{-1}, 440 cm^{-1}, and 365 cm^{-1}, corresponding to the modes A_g^2, B_{2g}, and A_g^1, respectively.[87] These findings align well with earlier observations conducted on bulk BP crystals. The distinctive mode represents the specific crystal structure of phosphorus known as orthorhombic, thereby affirming the orthorhombic nature of BP investigated in this study.[86]

**ADVANCED
SCIENCE NEWS**

www.advancedsciencenews.com

**ADVANCED
ELECTRONIC
MATERIALS**

www.advelectronicmat.de

Figure 13. a) Power spectra of freestanding monolayer black phosphorus calculated in the temperature range of 4–300 K. Temperature dependence of frequency shift for freestanding monolayer black phosphorus, a) without and b) including the thermal expansion. Reproduced with permission.[102] Copyright 2019, American Chemical Society.

Similarly, Raman spectroscopy has been employed to study the anisotropy of GeSe with different lattice orientations.[88] By rotating the sample at specific intervals and integrating a linear polarizer into the detection systems,[88,89] researchers measured the polarization in both parallel and perpendicular setup relative to the incident light's polarization.[91] The study showed that three phonon peak intensities of the A_g^1, B_{3g}, and A_g^3 modes exhibit strong angular dependence under different polarized configurations. Under the parallel or cross-polarized configuration, the corresponding contour color map, as well as a sequence of Raman spectra for GeSe nanoflakes at various rotation angles, can be observed in Figure 5h,i.
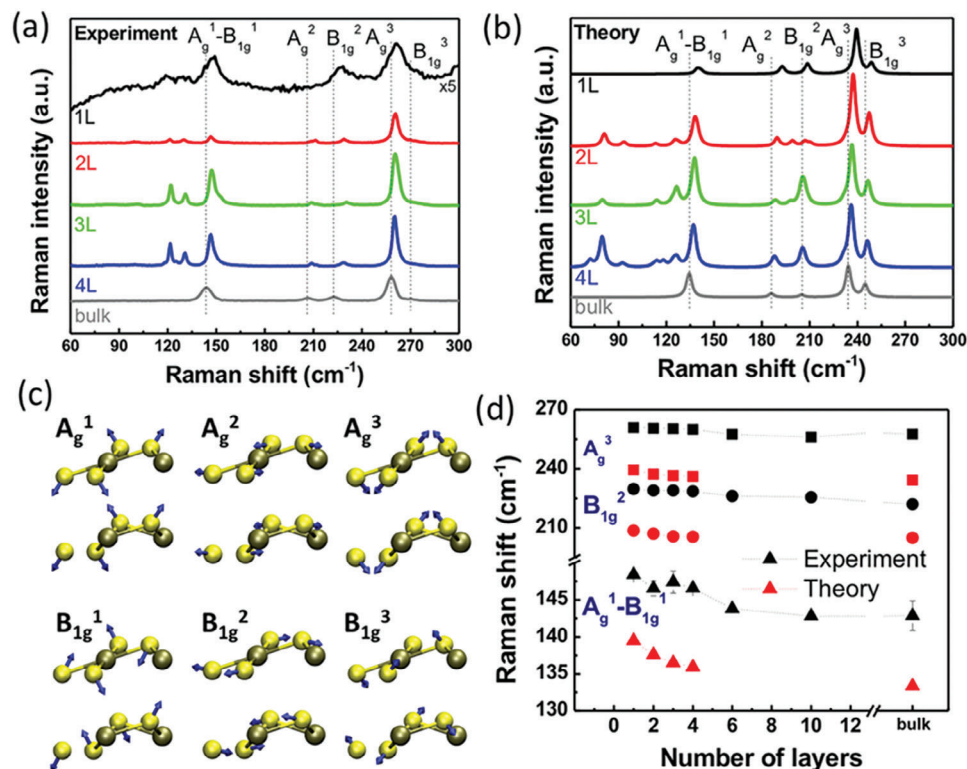
Gu reported two structures of $PdSe_2$, O-$PdSe_2$ and M-$PdSe_2$, and the anisotropy of M-$PdSe_2$ is tested in detail here.[92] **Figure 6a** illustrates the measurement of Raman spectra for M-$PdSe_2$ under 532 nm laser excitation. The parallel configuration $z(xx)\bar{z}$ was employed for polarization. The crystal orientation of the a-axis was set at 0° with respect to the laser polarization. Figure 6b–g illustrates the acquisition of Raman spectra from different angle by rotating the sample within a plane and b plane, with 10° increments. Six Raman peaks are observed at different wavenumbers from 159.8 cm^{-1} to 227.4 cm^{-1}. It is noteworthy that the polar plots display distinct bowknot shapes for both the

Raman peak at 159.8cm^{-1} and the Raman peak at 227.4cm^{-1}, whereas the polar plot of the Raman peak at 192.8 cm^{-1} demonstrates heightened intricacy. Due to the complexity of the phase angle, the phase angle difference Φba, (Φba is the phase angle difference between b and a, the phase difference). determines the position of the angle with the lowest intensity. The lowest intensity can be found at either 0° or 90°, resulting in the highest intensity occurring at 90° or 0°, the polar plot exhibits a bow-tie shape similar to that of the 159.8 cm^{-1} peaks and 227.4 cm^{-1} peaks. However, when considering specific values of Φba, the angle range of 0° to 90° exhibits the lowest intensity, while the angles of 0° and 90° manifest as the angles of highest intensity and second highest intensity, which can interchange their positions.

Qiu et al. studied angle-resolved Raman spectra of $ZrTe_5$ at room temperature.[93] **Figure 7** below shows the angle-dependent Raman spectra of $ZrTe_5$ in this setup. They extracted the intensities of the six main peaks and plotted them as polar plots in Figure 7b–g. As well as the results for the ac (polarizer perpendicular to the incident light) configuration.

Song and his team conducted a comprehensive investigation into the in-plane anisotropy of Raman modes in both few-layer and bulk WTe_2,[94] utilizing angle-dependent and polarized

**ADVANCED
SCIENCE NEWS**

www.advancedsciencenews.com

**ADVANCED
ELECTRONIC
MATERIALS**

www.advelectronicmat.de

Figure 14. a) Ranging from monolayer to bulk, the Raman spectrum of $PdSe_2$ was acquired in experiments using a laser with 532 nm for excitation. b) Employing the optPBE method, the corresponding theoretical Raman spectrum was calculated, spanning from 1L to bulk. a,b), dashed lines indicate the positions of Raman peaks denoting bulk $PdSe_2$. It's worth noting that the convergence of A_g^1 and B_{1g}^1 peaks is represented by the label A_g^1-B_{1g}^1. c) Presented are the atomic displacements (indicated by blue arrows) of these six different modes of Raman spectrum in bulk $PdSe_2$. d) These three modes: A_g^1-B_{1g}^1, B_{1g}^2, and A_g^3 are compared at different thicknesses[124] considering both the experimental in black and theoretical in red results. The frequency shift trend versus thickness is consistent, despite the calculated frequencies consistently being slightly smaller than the experimental ones. Reproduced with permission.[124] Copyright 2017, American Chemical Society.

Raman spectroscopy. **Figure 8** below clearly displays the resolution of ten distinct Raman modes. Moreover, the impact of material absorption on high-frequency phonon modes was examined, and the analysis took into account the intricate elements of the Raman tensor.
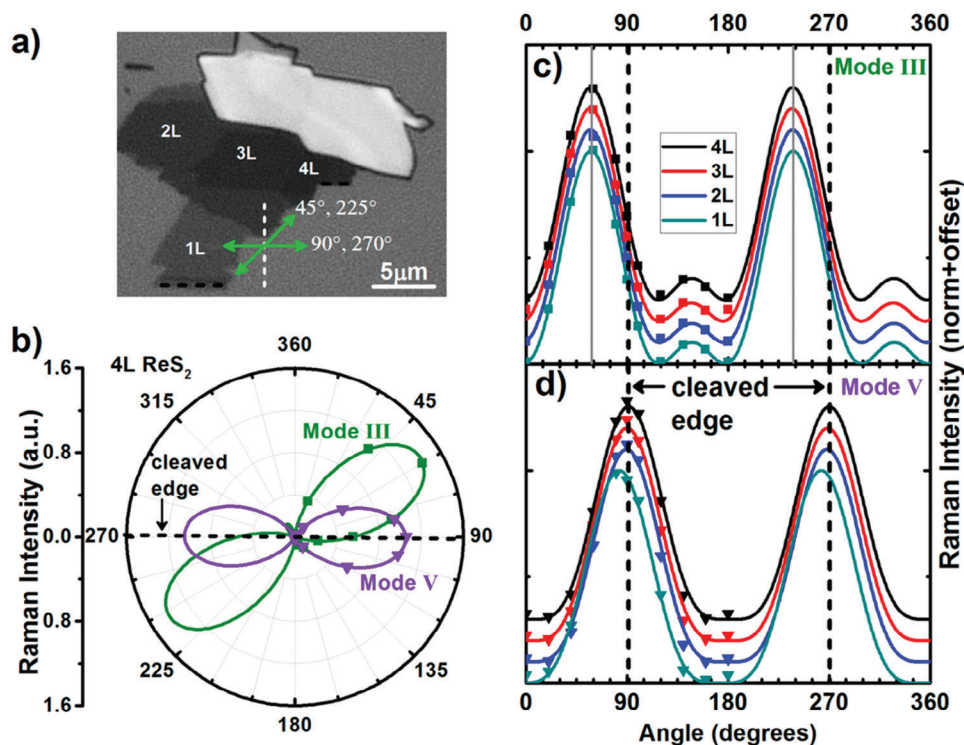
4.2. Interlayer Coupling

Interlayer coupling in 2D materials signifies the interaction between different layers, profoundly influencing the material's electronic structure and physical attributes. It is essential to note that interlayer coupling in 2D materials isn't solely dictated by the interlayer distance. The stacking order or arrangement of these layers significantly influences this coupling as well. Researchers have extensively employed low-frequency (LF) interlayer Raman spectroscopy and angle-resolved Raman spectroscopy to study interlayer coupling in isotropic 2D materials. For instance, Wu et al.,[94] used the resonant Raman spectroscopy to elucidate the stacking order in twisted multilayer graphene and established that different stacking sequences led to distinct phonon dispersions. Yan and colleagues[95] demonstrated how polarization Raman spectroscopy can be a valuable tool in determining the interlayer interactions and stacking configurations in

TMDs. However, when venturing into anisotropic 2D materials, much of the focus has predominantly zeroed in on the in-plane anisotropy.

Qiao et al. first measured the rigid layer pattern of NL ReS_2 (N > 2) using ultra-low- and high-frequency Raman spectroscopy. **Figure 9a,b** shows the high-frequency Raman spectra of 1–8 layers of ReS_2 in different stacking modes. Pos(mb)– Pos(ma) increases from 16.7 cm^{-1} of 1L ReS2 to 20.6 cm^{-1} of AI-8L-ReS_2, but decreases to 13.3 cm^{-1} of IS-8L-ReS_2, as plotted in Figure 9c.[97] This explicit difference in the observed frequencies identifies an unexpectedly strong interlayer coupling in IS- and AI-NL-ReS_2. Zhao et al.[97] delved into the Raman vibrational modes of $ReSe_2$, with a specific focus on interlayer and intralayer modes, elaborating on the associated Raman tensor and polarization dependencies. The reduced in-plane symmetry of the $ReSe_2$ lattice means that the intensities of the interlayer shear (C) and layer-breathing (LB) Raman modes are strongly influenced by the polarization angle of the incident laser beam. This accentuates the interlayer coupling features and the anisotropic interlayer vibration modes in $ReSe_2$. In contrast, the intralayer Raman modes pertain to the intra-layer phonon vibrations in layered materials. The layer-number dependence of high-frequency Raman modes (>50 cm^{-1}) can also shed light on interlayer interactions in 2D materials. Similarly, the reduced in-plane symmetry results in a

**ADVANCED
SCIENCE NEWS**

www.advancedsciencenews.com

**ADVANCED
ELECTRONIC
MATERIALS**

www.advelectronicmat.de

Figure 15. a) The Raman spectra ranging from 1L to 4L ReS$_2$ are presented in a stacked plot, with the sample oriented at $\theta = 120°$. b) In a polar plot, the angle-resolved Raman intensities of modes III (green squares) and V (purple triangles) are displayed for a 4L ReS$_2$ sample. c) The intensity of mode III varies with sample orientation across 1L-4L thickness samples. The plot shows normalized and offset data for each layer thickness. The solid gray lines indicate the angle of maximum intensity. d) Mode V exhibits a similar behavior as described in (c). Reproduced with permission.[125] Copyright 2015, American Chemical Society.

pronounced polarization dependence for the intralayer Raman modes in ReSe$_2$.

4.3. Bandgap Dependence

A salient feature in Raman's studies of 2D materials is the interplay between phonons and electronic bands. Specifically, the intensity and position of phonon scattering in Raman spectra can be influenced by the electronic band structure of the material. For instance, when electronic transitions occur within specific bands, they can modulate certain phonon modes, either amplifying or attenuating their signatures in the Raman spectrum. Such a phenomenon is particularly evident in materials where electron–phonon coupling is pronounced.

Li et al. employed ARPRS to investigate the vibrational anisotropy of GeAs$_2$.[99] To achieve this, a linear polarizer was rotated in front of the Raman detector, allowing the collection of scattered signals from polarization states that were either parallel or perpendicular to the polarization direction of the incident light. In addition to Raman spectroscopy, the anisotropy of GeAs$_2$ can also be clearly observed from the energy band. **Figure 10**c–g displays the different vibration modes found in the energy band.
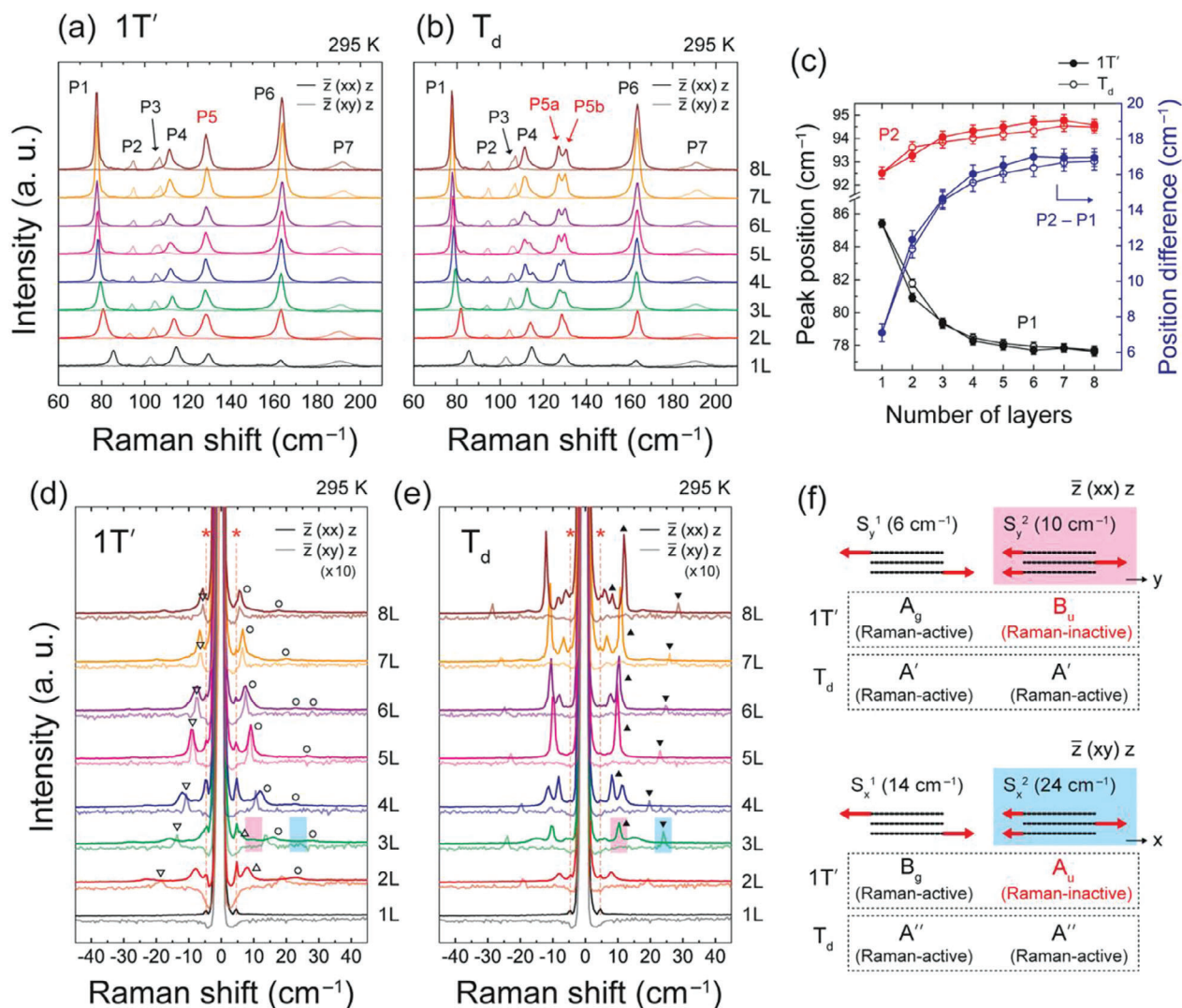
Ling et al. to analyze the anisotropy of electron–phonon interaction, based on the band structures of monolayer, bilayer, trilayer, and bulk BP, as well as the symmetry assignments for all bands at the Γ point. They found that the different BP thick-

nesses, the electron band structures, as well as the symmetry assignments for each band, are different.[81] **Figure 11**b,c shows two typical examples of the optical absorption for trilayer BP with EL = 0.82 eV and EL = 4.33 eV, respectively.

4.4. Temperature Dependence

Temperature-induced changes in 2D materials can markedly influence phonon–phonon interactions. As temperature rises, there's an increase in lattice vibrations, leading to alterations in the phonon density of states. Consequently, the frequency, width, and intensity of the Raman peaks associated with specific phonon modes may change. Such changes are often attributed to various mechanisms, including phonon–phonon scattering, anharmonic effects, and changes in the electron–phonon coupling. Zhang et al. conducted temperature-dependent Raman measurements on nano-ZrTe$_5$[100], revealing a clear temperature-dependence of ZrTe$_5$ grown using the CVT method. The Raman spectra of ZrTe$_5$ are presented below, covering a temperature range of 100–300 K. The Raman shifts and the full width at half maximum of the B$_{1g}$ peak is displayed, both of which vary with temperature. These measurements show distinct phonon modes, such as B$_{2g}$ and A$_g$, confirming their characteristic nature, consistent with previous studies **Figure 12**.

Damien Tristant et al., have demonstrated through DFT calculations that the frequency drop is mainly caused by phonon–

**ADVANCED
SCIENCE NEWS**

www.advancedsciencenews.com

**ADVANCED
ELECTRONIC
MATERIALS**

www.advelectronicmat.de

Figure 16. In the frequency range of 60 to 210 cm^{-1}, two distinct phases of MoTe$_2$ exhibit a polarized Raman spectrum: a) the 1T′phase and b) the T_d phase. Two distinct configurations are depicted here, represented by contrasting light and dark lines. The dependence of the peak positions of P1 and P2 and their difference in the thickness is shown in (c). Raman spectra with low-frequency polarization are observed for MoTe$_2$ in the d) 1T′phase and e) T_d phase. A schematic representation of interlayer shear modes in 3L MoTe$_2$ is shown in (f). Reproducedwith permission.[46] Copyright 2021, American Chemical Society.
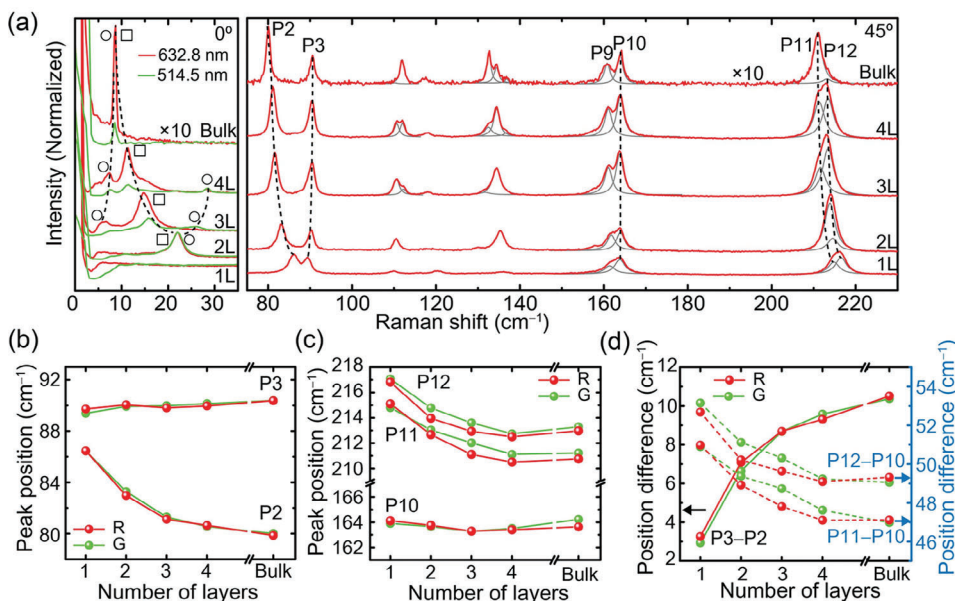
phonon scattering, while thermal expansion only acts indirectly by re-normalizing phonon–phonon scattering **Figure 13**.[102]

4.5. Thickness Dependence

Within a Raman spectrum, the frequency, intensity, and width of specific vibrational modes can provide clear signatures corresponding to a particular layer number. For instance, in graphene, the position and intensity ratio of the G and 2D peaks serve as reliable indicators for layer number identification. A single layer of graphene showcases a sharp and pronounced 2D peak, while bilayer graphene demonstrates a broader and less intense 2D peak, and so on for multiple layers. Beyond mere identification, the number of layers can profoundly influence various physical properties of the material. In TMDs like MoS$_2$, monolayers exhibit direct bandgap behavior, making them suitable for optoelectronic applications, whereas bilayers or more manifest an indirect bandgap, steering their utility toward other functionalities. This transition is underpinned by changes in electronic band structure as the layer number varies. Moreover, interlayer interactions become increasingly prominent as more layers are added. This can lead to the emergence of new Raman-active modes, a phenomenon observable in several 2D materials, indicative of the layers' collective vibrational behavior.

According to the atomic displacement of lattice vibrations, there are two kinds of Raman modes in 2DMs, intralayer and interlayer modes, stemming from intralayer chemical bonds and layer-layer vdW interaction, respectively.[103] The

**ADVANCED
SCIENCE NEWS**

www.advancedsciencenews.com

**ADVANCED
ELECTRONIC
MATERIALS**

www.advelectronicmat.de

Figure 17. Thickness dependence of Raman spectrum of WTe_2. a) Raman spectrum as a function of thickness of WTe_2, measured with excitation wavelength of 632.8 nm. For the low-frequency region, the spectra measured with 514.5 nm excitation are also shown. The Raman spectrum of bulk WTe2 is magnified 10 times. Thickness dependence of b) P2 and P3 and c) P10, P11, and P12 peak positions. d) Thickness dependence of peak position differences between P2 and P3; P10 and P11; and P10 and P12. Reproduced with permission.[127] Copyright 2016, Royal Society of Chemistry.

features of intralayer Raman modes provide information of compositions and structural phase. Their response to external perturbation provides opportunities to investigate fundamental properties of 2DMs, such as temperature dependence for phonon anharmonicity, electron–phonon coupling (EPC) and thermal expansion,[103,104] electrostatic doping dependence for EPC,[105,106] strain dependence for elastic constant,[107,108] defect concentration dependence for phonon confinement effect,[109–112] magnetic field dependence for Fermi velocity and many-body effect,[113,114] and excitation energy (E_{ex}) dependence for band structure, double resonance Raman process,[115,116] interlayer EPC[118] and phonon dispersion.[118–120] The interlayer Raman modes involve layer–layer vibration where each layer can be treated as a whole unit, which is known as linear chain model (LCM) for Raman spectroscopy.[102,121,122] Based on the low-frequency Raman technique developed by Tan et al.[103] the interlayer Raman modes of 2DMs can be observed easily. This stimulates huge interest to investigate the interlayer coupling in 2DMs and related vdWHs, which is highly sensitive to the thickness and stacking order of 2DM flakes[98]
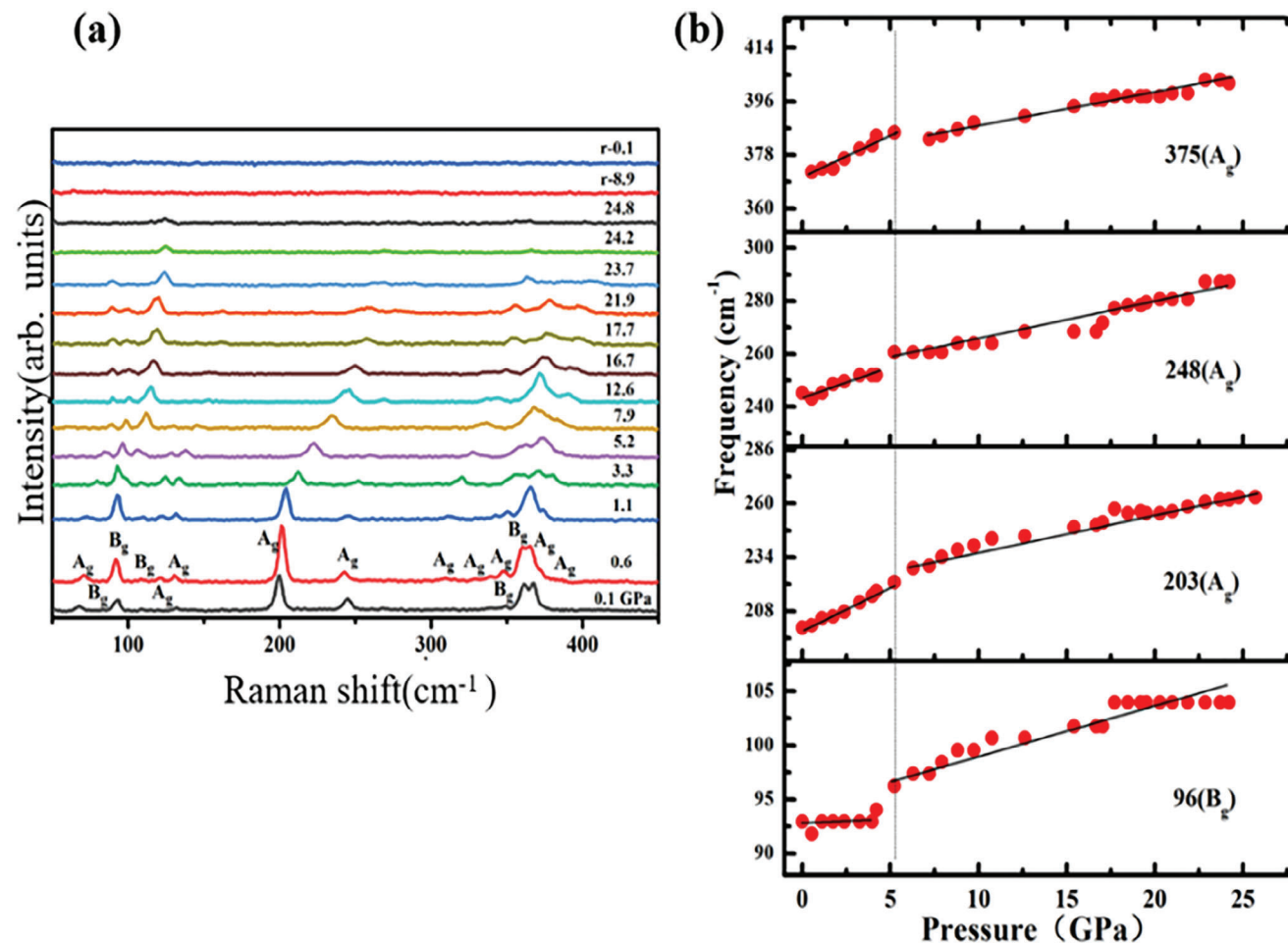
Akinola D. Oyedele's group conducted characterizations of $PdSe_2$ anisotropy[124] **Figure 14a** displays the unpolarized Raman spectrum, where only the A_g modes and B_{1g} modes are observable. This aligns with the theoretical Raman spectroscopy outcome shown in Figure 14b. Despite the presence of A_g^1, A_g^2, and A_g^3 modes and B_{1g}^1, B_{1g}^2, and B_{1g}^3 modes in bulk $PdSe_2$, calculations indicate a close proximity between A_g^1 and B_{1g}^1 modes, with a frequency difference of less than 2 cm^{-1}. Consequently, a single mixed peak (A_g^1- B_{1g}^1) emerges at ≈145 cm^{-1} in the measurements. Figure 14c illustrates the atomic vibrations of the six different Raman modes of $PdSe_2$, highlighting the predominant

participation of Se atoms (represented by blue arrows). This feature arises from the distinct structural properties of $PdSe_2$.

Daniel et al. demonstrated that polarized Raman scattering can determine the orientation of ReS_2 and resolve the angular Raman intensity of different modes in ReS_2 samples.[125] This experimental phenomenon examined the coherence of Raman polarization and the dependence of each mode on layer thickness. **Figure 15b** shows the polarization characteristics of mode III for 1L, 2L, 3L, and 4L. In these regions, mode III maintains constant polarization across various thicknesses, with its highest intensity at ≈58°. Unlike mode III, mode V shows slight variations in polarization with thickness, reaching its peak intensity at 83° for 1L, 90° for 2L, and 91° for both 3L and 4L configurations, as depicted in Figure 15c. These two modes were previously calculated in the literature by DFT simulations.[124–126] Mode III primarily consists of in-plane vibrations, while Mode V comprises both out-of-plane vibrations of the sulfur atoms and in-plane vibrations of the rhenium atoms along the *b*-axis. The authors hypothesized that the angle of maximum intensity for Mode V aligns with the *b*-axis direction. Possible factors contributing to this variation include interlayer mating, interactions with the substrate, and induced strain from the mechanical peeling procedure. These effects are expected to diminish with each subsequent layer. On the other hand, Cheon studied the phase transition of $MoTe_2$ and performed a series of Raman spectra to characterize it.[46] The Raman characterization of the 1T′ phase and T_d phase was carried out in different polarization configurations, respectively **Figure 16**.

Kim's team used polarization Raman spectroscopy to determine the thickness of the WTe_2 sample and performed a detailed analysis **Figure 17**.[126]

**ADVANCED
SCIENCE NEWS**

www.advancedsciencenews.com

**ADVANCED
ELECTRONIC
MATERIALS**
Open Access

www.advelectronicmat.de

Figure 18. a) The Raman spectrum and b) the Raman frequency under varying pressure were analyzed. The experimental data is represented by dots, while the linear fitting outcomes in (b) are depicted by lines. Reproduced with permission.[128] Copyright 2022, AIP Publishing.

4.6. High-Pressure Phase Transition

As pressure is applied, 2D materials may undergo structural rearrangements or transformations. These changes are often accompanied by shifts in vibrational frequencies, emergence or disappearance of specific Raman modes, or alterations in peak intensities and widths. For example, the shift in characteristic Raman peaks can give insights into the pressure-induced changes in bond lengths and bond angles. Beyond structural transitions, high pressure can also affect electron–phonon interactions in 2D materials. Such changes can be deduced from the Raman peak intensities and their pressure-dependent shifts. Furthermore, the coupling between different vibrational modes may result in the appearance of combination or overtone modes under high-pressure conditions, revealing the intricacies of phonon interactions.

High-pressure Raman spectroscopy is a powerful tool for characterizing anisotropic 2D materials, even uncovering anisotropy that may not be apparent under normal conditions. For instance, in the case of GeP, Tao et al. utilized high-pressure Raman spectroscopy to investigate its structural changes under pressure (see

Figure 18), providing valuable insights into its crystal structure and phonon properties.[127]

Similarly, Xia et al. employed Raman spectroscopy and calculations to study the high-pressure properties of WTe$_2$ crystals.[129] They conducted a series of Raman spectroscopic studies on bulk T_d-WTe$_2$, focusing on its anisotropy in both parallel and vertical directions. They classified the orientations of the ab plane of WTe$_2$ relative to the diamond anvil cell as P-type when parallel and V-type when perpendicular. The Raman spectra revealed distinct behavior between the P and V types, particularly a significant envelope peak at ≈120 cm^{-1} in the V-type configuration. As pressure increased, the lattice vibrational properties of the P-type gradually exhibited a blueshift without any structural phase transitions throughout the pressure range examined, up to 17.0 GPa **Figure** 19.

5. Summary and Outlook

The main objective of this review is to provide a comprehensive summary of various configurations of anisotropic materials in two dimensions. The point symmetry of anisotropic 2D materials is briefly summarized, and propose a categorization for

2300610 (16 of 20)
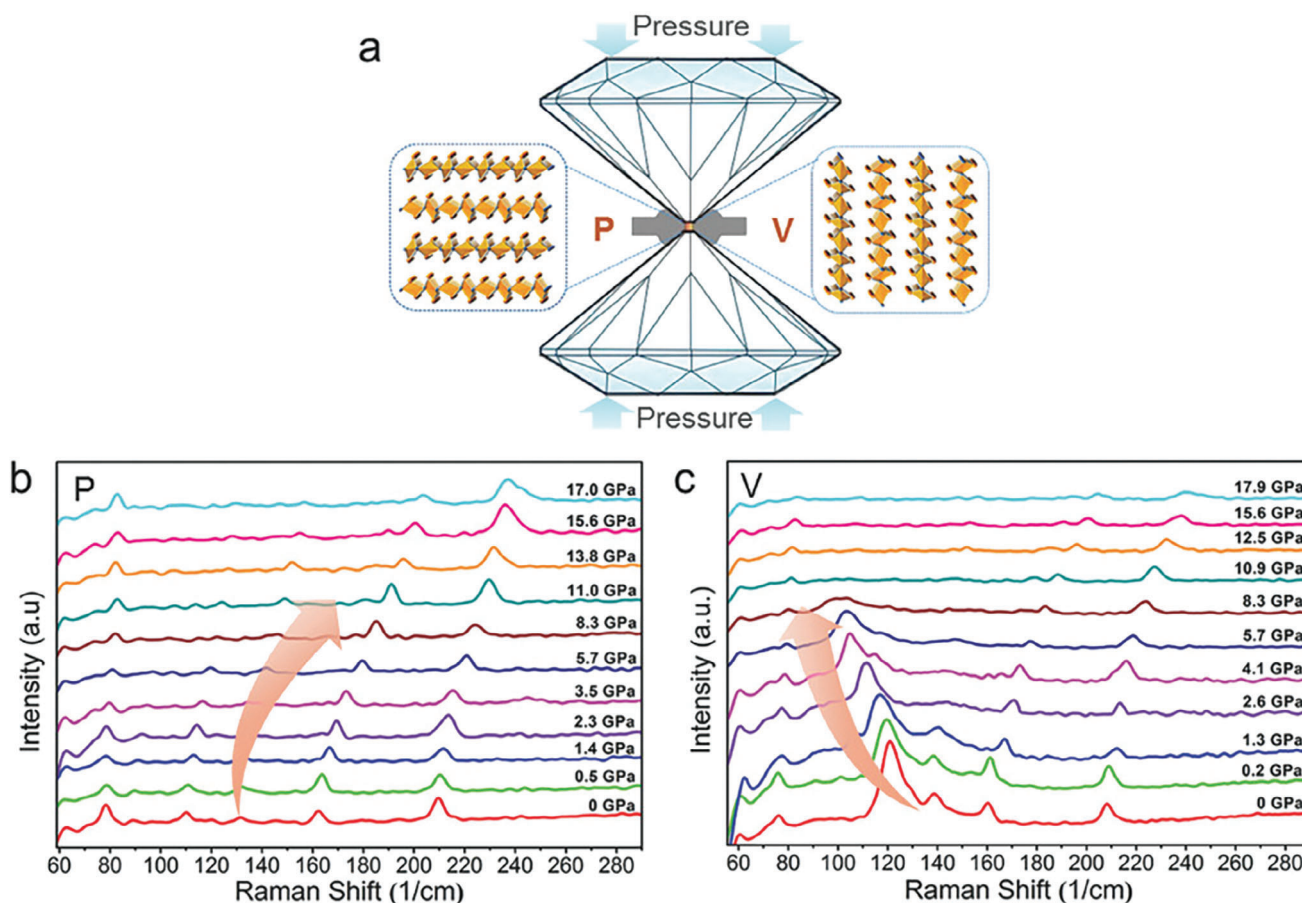
Figure 19. a) WTe$_2$ crystals are loaded into a diamond anvil cell, arranged both in a parallel (P) configuration and vertically aligned (V). The images depict the configuration. b,c) The Raman vibration's response to pressure is examined for various crystal orientations, illustrating its evolution. Reproduced with permission.[129] Copyright 2017, John Wiley and Sons.

them. The equipment configurations for Raman spectroscopy are discussed, and we summarize the diverse Raman spectroscopic characterizations of different materials. We also explore the application of Raman spectroscopy, including Polarization Raman and its equipment, orientation identification, interlayer coupling, bandgap, temperature, thickness, and high-pressure dependence of Raman, to characterize different characteristic anisotropic materials.

Currently, the development of 2D anisotropic materials faces challenges, particularly in their preparation. Selenium and telluride samples are predominantly obtained through mechanical exfoliation. While research on anisotropic devices primarily focuses on black phosphorus materials, there is a notable scarcity of studies on novel 2D materials based on transition metal sulfides and selenides. However, by comparing the crystal structures and properties of different 2D materials, we can infer similarities in their behavior.

As research on anisotropic 2D materials continues, we expect these materials to find applications in a wider range of fields. Further investigation into the diverse anisotropy arising from different material structures is essential. Introducing defects can be a means to achieve desired anisotropic properties, and exploring combinations of 2D materials

with metallic materials is another promising direction. Additionally, researchers may explore the possibility of tuning anisotropy for applications in flexible electronics or biomedical devices. With ongoing advancements, anisotropic 2D materials hold great potential for future technological innovations.

Conflict of Interest

The authors declare no conflict of interest.

Keywords

2D materials, anisotropy, Raman spectroscopy

[1] C. Gong, Y. Zhang, W. Chen, J. Chu, T. Lei, J. Pu, L. Dai, C. Wu, Y. Cheng, T. Zhai, L. Li, J. Xiong, *Adv. Sci.* **2017**, *4*, 1700231.

**ADVANCED
SCIENCE NEWS**

www.advancedsciencenews.com

**ADVANCED
ELECTRONIC
MATERIALS**

www.advelectronicmat.de

[2] H. Tian, J. Tice, R. Fei, V. Tran, X. Yan, L. Yang, H. Wang, *Nano Today* **2016**, *11*, 763.

[3] X. Liu, C. R. Ryder, S. A. Wells, M. C. Hersam, *Small Methods* **2017**, *1*, 1700143.

[4] R. Fei, W. Li, J. Li, L. Yang, *Appl. Phys. Lett.* **2015**, *107*, 173104.

[5] H. Yuan, X. Liu, F. Afshinmanesh, W. Li, G. Xu, J. Sun, B. Lian, A. G. Curto, G. Ye, Y. Hikita, Z. Shen, S.-C. Zhang, X. Chen, M. Brongersma, H. Y. Hwang, Y. Cui, *Nat. Nanotechnol.* **2015**, *10*, 707.

[6] Z.-D. Gao, Z.-H.-Y. Jiang, J.-D. L. B.-W. Li, Y.-Y. Long, X.-M. Li, J. Yin, W.-L. Guo, *Adv. Eng. Mater.* **2022**, *24*, 2200519.

[7] R. Zhu, Z. Gao, Q. Liang, J. Hu, J.-S. Wang, C.-W. Qiu, A. T. S. Wee, *ACS Appl. Mater. Interfaces* **2021**, *13*, 37527.

[8] Y. Zhang, J. Liu, S. Cheng, X. Guo, R. Huang, H. Ke, T. Lin, X. Zhang, *Nat. Sci.* **2023**, *62*, 209.

[9] D. Xie, J. Jiang, L. Ding, *J. Semicond.* **2022**, *43*, 010201.

[10] S. Zhao, P. Luo, S. Yang, X. Zhou, Z. Wang, C. Li, S. Wang, T. Zhai, X. Tao, *Adv. Opt. Mater.* **2021**, *9*, 2100198.

[11] Z. Wang, P. Luo, B. Han, X. Zhang, S. Zhao, S. Wang, X. Chen, L. Wei, S. Yang, X. Zhou, S. Wang, X. Tao, T. Zhai, *ACS Nano* **2021**, *15*, 20442.

[12] J. Guo, Z. Xiao, Z. Wu, X. Liao, S. Wan, X. Fu, Y. Zhou, *Adv. Opt. Mater.* **2022**, *10*, 2201030.

[13] X. Xie, J. Ding, B. Wu, H. Zheng, S. Li, C.-T. Wang, J. He, Z. Liu, J.-T. Wang, J.-A. Duan, Y. Liu, *Nanoscale* **2023**, *15*, 12388.

[14] J. Qiao, F. Feng, Z. Wang, M. Shen, G. Zhang, X. Yuan, M. G. Somekh, *ACS Appl. Mater. Interfaces* **2021**, *13*, 17948.

[15] F. Chen, G. Liu, Z. Xiao, H. Zhou, L. Fei, S. Wan, X. Liao, J. Yuan, Y. Zhou, *ACS Appl. Mater. Interfaces* **2023**, *15*, 16999.

[16] Z. Guo, R. Cao, H. Wang, X. Zhang, F. Meng, X. Chen, S. Gao, D. K. Sang, T. H. Nguyen, A. T. Duong, J. Zhao, Y.-J. Zeng, S. Cho, B. Zhao, P.-H. Tan, H. Zhang, D. Fan, *Natl. Sci. Rev.* **2022**, *9*, nwab098.

[17] A. Dasgupta, J. Gao, X. Yang, *npj 2D Mater. Appl.* **2021**, *5*, 74.

[18] G. Li, H. Zhang, Y. Li, S. Yin, X. Kan, W. Wei, H. Du, B. Ge, C. An, M. Tian, F. Yan, S. Yang, T. Zhai, L. Li, *Nano Res.* **2022**, *15*, 5469.

[19] R. Zhang, Y. Wei, Y. Kang, M. Pu, X. Li, X. Ma, X. Xu, X. Luo, *Adv. Sci.* **2022**, *9*, 2103429.

[20] Q. Zhang, S. Tan, R. G. Mendes, Z. Sun, Y. Chen, X. Kong, Y. Xue, M. H. Rümmeli, X. Wu, S. Chen, L. Fu, *Adv. Mater.* **2016**, *28*, 2616.

[21] F. Qi, Y. Chen, B. Zheng, J. He, Q. Li, X. Wang, J. Lin, J. Zhou, B. Yu, P. Li, W. Zhang, *Appl. Surf. Sci.* **2017**, *413*, 123.

[22] J. A. Aliaga, T. Zepeda, J. F. Araya, F. Paraguay-Delgado, E. Benavente, G. Alonso-Nunez, S. Fuentes, G. Gonzalez, **2017**, *Catalysts 7*, 337.

[23] J. Gao, L. Li, J. Tan, H. Sun, B. Li, J. C. Idrobo, C. V. Singh, T.-M. Lu, N. Koratkar, *Nano Lett.* **2016**, *16*, 3780.

[24] C. Feng, Z.-P. Wu, K.-W. Huang, J. Ye, H. Zhang, *Adv. Mater.* **2022**, *34*, 2200180.

[25] T. Yu, C. Wang, X. Yan, G. Yang, U. Schwingenschlögl, *J. Phys. Chem. Lett.* **2021**, *12*, 2464.

[26] Y. Lu, K. Xu, M.-Q. Yang, S.-Y. Tang, T.-Y. Yang, Y. Fujita, S. Honda, T. Arie, S. Akita, Y.-L. Chueh, K. Takei, *Nanoscale Horiz.* **2021**, *6*, 260.

[27] K. Yin, L. Wang, Q. Deng, Q. Huang, J. Jiang, G. Li, J. He, *Nano-Micro Lett.* **2022**, *14*, 97.

[28] Z. Yin, K. C. Xu, S. Z. Jiang, D. Luo, R. Chen, C. X. Xu, P. Shum, Y. J. Liu, *Mater. Today Phys.* **2021**, *18*, 100378.

[29] R. Fei, L. Yang, *Nano Lett.* **2014**, *14*, 2884.

[30] R. Fei, A. Faghaninia, R. Soklaski, J.-A. Yan, C. Lo, L. Yang, *Nano Lett.* **2014**, *14*, 6393.

[31] L. C. Gomes, A. Carvalho, *Phys. Rev. B* **2015**, *92*, 085406.

[32] J. Carrete, N. Mingo, S. Curtarolo, *Appl. Phys. Lett.* **2014**, *105*, 101907.

[33] G. Shi, E. Kioupakis, *Nano Lett.* **2015**, *15*, 6926.

[34] C. W. Li, J. Hong, A. F. May, D. Bansal, S. Chi, T. Hong, G. Ehlers, O. Delaire, *Nat. Phys.* **2015**, *11*, 1063.

[35] L.-D. Zhao, S.-H. Lo, Y. Zhang, H. Sun, G. Tan, C. Uher, C. Wolverton, V. P. Dravid, M. G. Kanatzidis, *Nature* **2014**, *508*, 373.

[36] X. Cui, W. Dong, S. Feng, G. Wang, C. Wang, S. Wang, Y. K. Zhou, X. H. Qiu, L. Q. Liu, Z. P. Xu, Z. Zhang, *Small* **2023**, *19*, 2301959.

[37] J.-K. Qin, C. Sui, Z. Qin, J. Wu, H. Guo, L. Zhen, C.-Y. Xu, Y. Chai, C. Wang, X. He, P. D. Ye, J. Lou, *Nano Lett.* **2021**, *21*, 8043.

[38] T. Wen, M. Zhang, J. Li, C. Jiao, S. Pei, Z. Wang, J. Xia, *Nanoscale Horiz.* **2023**, *8*, 516.

[39] F. Q. Wang, S. Zhang, J. Yu, Q. Wang, *Nanoscale* **2015**, *7*, 15962.

[40] L. S. Lu, G. H. Chen, H. Y. Cheng, C. P. Chuu, K. C. Lu, C. H. Chen, M. Y. Lu, T. H. Chuang, D. H. Wei, W. C. Chueh, W. B. Jian, M. Y. Li, Y. M. Chang, L. J. Li, W. H. Chang, *ACS Nano* **2020**, *14*, 4963.

[41] N. T. Tien, P. T. B. Thao, N. H. Dang, N. D. Khanh, V. K. Dien, *Nanomaterials* **2023**, *13*, 1728.

[42] X. Chen, M.-L. Lin, X. Cong, Y.-C. Leng, X. Zhang, P.-H. Tan, *Carbon* **2021**, *185*, 282.

[43] X. Zhang, Q.-H. Tan, J.-B. Wu, W. Shi, P.-H. Tan, *Nanoscale* **2016**, *8*, 6435.

[44] X.-L. Li, W.-P. Han, J.-B. Wu, X.-F. Qiao, J. Zhang, P.-H. Tan, *Adv. Funct. Mater.* **2017**, *27*, 1604468.

[45] M. A. Pimenta, G. C. Resende, H. B. Ribeiro, B. R. Carvalho, *Phys. Chem. Chem. Phys.* **2021**, *23*, 27103.

[46] Y. Cheon, S. Y. Lim, K. Kim, H. Cheong, *ACS Nano* **2021**, *15*, 2962.

[47] F. Xia, H. Wang, J. C. M. Hwang, A. H. C. Neto, L. Yang, *Nat. Rev. Phys.* **2019**, *1*, 306.

[48] Z. Zhou, Y. Cui, P.-H. Tan, X. Liu, Z. Wei, *J. Semicond.* **2019**, *40*, 061001.

[49] A. D. Oyedele, S. Z. Yang, L. B. Liang, A. A. Puretzky, K. Wang, J. J. Zheng, P. Yu, P. R. Pudasaini, A. W. Ghosh, Z. Liu, C. M. Rouleau, B. G. Sumpter, M. F. Chisholm, W. Zhou, P. D. Rack, D. B. Geohegan, K. Xiao, *J. Am. Chem. Soc.* **2017**, *139*, 14090.

[50] T. Zhao, Y. Sun, Z. Shuai, D. Wang, *Chem. Mater.* **2017**, *29*, 6261.

[51] G. Manzoni, A. Sterzi, A. Crepaldi, M. Diego, F. Cilento, M. Zacchigna, P. Bugnon, H. Berger, A. Magrez, M. Grioni, F. Parmigiani, *Phys. Rev. Lett.* **2015**, *115*, 5.

[52] P. Hu, J. Zhang, M. Yoon, X.-F. Qiao, X. Zhang, W. Feng, P. Tan, W. Zheng, J. Liu, X. Wang, J. C. Idrobo, D. B. Geohegan, K. Xiao, *2D Nano Res.* **2014**, *7*, 694.

[53] L. Li, W. K. Wang, P. L. Gong, X. D. Zhu, B. Deng, X. Q. Shi, G. Y. Gao, H. Q. Li, T. Y. Zhai, *Adv. Mater.* **2018**, *30*, 9.

[54] Y. Feng, W. Zhou, Y. Wang, J. Zhou, E. Liu, Y. Fu, Z. Ni, X. Wu, H. Yuan, F. Miao, B. Wang, X. Wan, D. Xing, *Phys. Rev. B* **2015**, *92*, 054110.

[55] X. L. Ma, P. J. Guo, C. J. Yi, Q. H. Yu, A. M. Zhang, J. T. Ji, Y. Tian, F. Jin, Y. Y. Wang, K. Liu, T. L. Xia, Y. G. Shi, Q. M. Zhang, *Phys. Rev. B* **2016**, *94*, 8.

[56] K. K. Mishra, T. R. Ravindran, J. O. Island, E. Flores, J. R. Ares, C. Sanchez, I. J. Ferrer, H. S. J. van der Zant, A. Pawbake, R. Kanawade, A. Castellanos-Gomez, D. J. Late, *ACS Appl. Nano Mater.* **2020**, *3*, 8794.

[57] X. Ling, S. Huang, E. H. Hasdeo, L. Liang, W. M. Parkin, Y. Tatsumi, A. R. T. Nugraha, A. A. Puretzky, P. M. Das, B. G. Sumpter, D. B. Geohegan, J. Kong, R. Saito, M. Drndic, V. Meunier, M. S. Dresselhaus, *Nano Lett.* **2016**, *16*, 2260.

[58] H. Jiang, H. Shi, X. Sun, B. Gao, *ACS Photonics* **2018**, *5*, 2509.

[59] V. Tran, R. Soklaski, Y. Liang, L. Yang, *Phys. Rev. B* **2014**, *89*, 6.

[60] C. Y. Xie, S. L. Jiang, Y. L. Gao, M. Hong, S. Y. Pan, J. J. Zhao, Y. F. Zhang, *Small* **2020**, *16*, 9.

[61] A. V. Kuklin, H. Ågren, *Phys. Rev. B* **2019**, *99*, 7.

[62] M. N. Ali, J. Xiong, S. Flynn, J. Tao, Q. D. Gibson, L. M. Schoop, T. Liang, N. Haldolaarachchige, M. Hirschberger, N. P. Ong, R. J. Cava, *Nature* **2014**, *514*, 205.

[63] W.-D. Kong, S.-F. Wu, P. Richard, C.-S. Lian, J.-T. Wang, C.-L. Yang, Y.-G. Shi, H. Ding, *Appl. Phys. Lett.* **2015**, *106*, 4.

**ADVANCED
SCIENCE NEWS**

www.advancedsciencenews.com

**ADVANCED
ELECTRONIC
MATERIALS**

www.advelectronicmat.de

[64] Y. Pan, B. He, T. Helm, D. Chen, W. Schnelle, C. Felser, *Nat. Commun.* **2022**, *13*, 3909.

[65] I. Ozdemir, A. W. Holleitner, C. Kastl, O. Ü. Aktürk, *Sci. Rep.* **2022**, *12*, 16.

[66] S. Y. Wu, W. Pan, J. L. Zhang, C. L. Ma, Y. Shan, L. Z. Liu, *2D Surf. Interfaces* **2021**, *27*, 6.

[67] H. W. Wang, M. L. Chen, M. J. Zhu, Y. N. Wang, B. J. Dong, X. D. Sun, X. R. Zhang, S. M. Cao, X. X. Li, J. Q. Huang, L. Zhang, W. L. Liu, D. M. Sun, Y. Ye, K. P. Song, J. J. Wang, Y. Han, T. Yang, H. H. Guo, C. B. Qin, L. T. Xiao, J. Zhang, J. H. Chen, Z. Han, Z. D. Zhang, *Nat. Commun.* **2019**, *10*, 8.

[68] J. F. Sánchez-Royo, J. Pellicer-Porres, A. Segura, V. Muñoz-Sanjosé, G. Tobías, P. Ordejón, E. Canadell, Y. Huttel, *Phys. Rev. B* **2002**, *65*, 8.

[69] J. Sun, J. Leng, *Phys. Lett. A* **2019**, *383*, 125856.

[70] J. Dai, X. C. Zeng, *Angew. Chem., Int. Ed. Engl.* **2015**, *54*, 7572.

[71] H. Grimmeiss, A. Rabenau, H. Hahn, P. J. Z. f. E. Ness, *Ber. Bunsenges. Phys. Chem.* **1961**, *65*, 776.

[72] N. Tripathi, V. Pavelyev, P. Sharma, S. Kumar, A. Rymzhina, P. Mishra, *Mater. Sci. Semicond. Process.* **2021**, *127*, 105699.

[73] F. Ghasemi, R. Frisenda, E. Flores, N. Papadopoulos, R. Biele, D. Perez De Lara, H. S. J. Van Der Zant, K. Watanabe, T. Taniguchi, R. D'agosta, J. R. Ares, C. Sánchez, I. J. Ferrer, A. Castellanos-Gomez, *Nanomaterials* **2020**, *10*, 711.

[74] W. Liu, M. Liu, X. Liu, X. Wang, H. Teng, M. Lei, Z. Wei, Z. Wei, *Appl. Phys. Lett.* **2020**, *116*, 4.

[75] L. Liu, Z. Cheng, B. Jiang, Y. Liu, Y. Zhang, F. Yang, J. Wang, X.-F. Yu, P. K. Chu, C. Ye, *ACS Appl. Mater. Interfaces* **2021**, *13*, 30797.

[76] S. X. Liu, G. Li, F. Zhu, H. F. Huang, J. S. Lu, J. L. Qu, L. Li, Q. Wen, *Adv. Funct. Mater.* **2022**, *32*, 7.

[77] T. L. Chu, S. S. Chu, R. L. Ray, *J. Appl. Phys.* **1982**, *53*, 7102.

[78] L. Zhou, A. Ramiere, P. B. Chen, J. Y. Tang, Y. H. Wu, X. Lei, G. P. Guo, J. Q. He, H. T. He, *New J. Phys.* **2019**, *21*, 093009.

[79] C. Cong, T. Yu, H. Wang, *ACS Nano* **2010**, *4*, 3175.

[80] X. Ling, S. X. Huang, E. H. Hasdeo, L. B. Liang, W. M. Parkin, Y. Tatsumi, A. R. T. Nugraha, A. A. Puretzky, P. M. Das, B. G. Sumpter, D. B. Geohegan, J. Kong, R. Saito, V. Meunier, M. S. Dresselhaus, *Nano Lett.* **2016**, *16*, 4731.

[81] X.-L. Liu, X. Zhang, M.-L. Lin, P.-H. Tan, *Chin. Phys. B* **2017**, *26*, 067802.

[82] M.-L. Lin, Y.-C. Leng, X. Cong, D. Meng, J. Wang, X.-L. Li, B. Yu, X.-L. Liu, X.-F. Yu, P.-H. Tan, *Sci. Bull.* **2020**, *65*, 1894.

[83] J. Kim, J.-U. Lee, J. Lee, H. J. Park, Z. Lee, C. Lee, H. Cheong, *Nanoscale* **2020**, *12*, 10407.

[84] J. Wu, N. Mao, L. Xie, H. Xu, J. Zhang, *Angew. Chem., Int. Ed. Engl.* **2015**, *54*, 2366.

[85] F. Xia, H. Wang, Y. Jia, *Nat. Commun.* **2014**, *5*, 4458.

[86] Y. Akahama, M. Kobayashi, H. Kawamura, *Solid State Commun.* **1997**, *104*, 311.

[87] X. Wang, Y. Li, L. Huang, X.-W. Jiang, L. Jiang, H. Dong, Z. Wei, J. Li, W. Hu, *J. Am. Chem. Soc.* **2017**, *139*, 14976.

[88] M. Hafeez, L. Gan, H. Li, Y. Ma, T. Zhai, *Adv. Mater.* **2016**, *28*, 8296.

[89] E. Lorchat, G. Froehlicher, S. Berciaud, *ACS Nano* **2016**, *10*, 2752.

[90] X. Zhou, X. Z. Hu, B. Jin, J. Yu, K. L. Liu, H. Q. Li, T. Y. Zhai, *Adv. Sci.* **2018**, *5*, 149.

[91] Y. Gu, L. Zhang, H. Cai, L. Liang, C. Liu, A. Hoffman, Y. Yu, A. Houston, A. A. Puretzky, G. Duscher, P. D. Rack, C. M. Rouleau, X. Meng, M. Yoon, D. B. Geohegan, K. Xiao, *ACS Nano* **2022**, *16*, 13900.

[92] G. Qiu, Y. Du, A. Charnas, H. Zhou, S. Jin, Z. Luo, D. Y. Zemlyanov, X. Xu, G. J. Cheng, P. D. Ye, *Nano Lett.* **2016**, *16*, 7364.

[93] Q. Song, X. Pan, H. Wang, K. Zhang, Q. Tan, P. Li, Y. Wan, Y. Wang, X. Xu, M. Lin, X. Wan, F. Song, L. Dai, *Sci Rep.* **2016**, *6*, 29254.

[94] J.-B. Wu, X. Zhang, M. Ijäs, W.-P. Han, X.-F. Qiao, X.-L. Li, D.-S. Jiang, A. C. Ferrari, P.-H. Tan, *Nat. Commun.* **2014**, *5*, 5309.

[95] J. X. Yan, J. Xia, X. L. Wang, L. Liu, J. L. Kuo, B. K. Tay, S. S. Chen, W. Zhou, Z. Liu, Z. X. Shen, *Nano Lett.* **2015**, *15*, 8155.

[96] X.-F. Qiao, J.-B. Wu, L. Zhou, J. Qiao, W. Shi, T. Chen, X. Zhang, J. Zhang, W. Ji, P.-H. Tan, *Nanoscale* **2016**, *8*, 8324.

[97] L. Liang, J. Zhang, B. G. Sumpter, Q.-H. Tan, P.-H. Tan, V. Meunier, *ACS Nano* **2017**, *11*, 11777.

[98] L. Li, P. Gong, D. Sheng, S. Wang, W. Wang, X. Zhu, X. Shi, F. Wang, W. Han, S. Yang, K. Liu, H. Li, T. Zhai, *Adv. Mater.* **2018**, *30*, 1804541.

[99] Y.-Y. Zhang, C. Di, Y.-Y. Lv, S.-T. Dong, J. Zhou, S.-H. Yao, Y. B. Chen, M.-H. Lu, Y.-F. Chen, *Cryst. Growth Des.* **2019**, *20*, 680.

[100] T. Jena, M. T. Hossain, P. K. Giri, *J. Mater. Chem. C* **2021**, *9*, 16693.

[101] D. Tristant, A. Cupo, X. Ling, V. Meunier, *ACS Nano* **2019**, *13*, 10456.

[102] X. Zhang, W. P. Han, J. B. Wu, S. Milana, Y. Lu, Q. Q. Li, A. C. Ferrari, P. H. Tan, *Phys. Rev. B* **2013**, *87*, 8.

[103] H.-N. Liu, X. Cong, M.-L. Lin, P.-H. Tan, *Carbon* **2019**, *152*, 451.

[104] N. Bonini, M. Lazzeri, N. Marzari, F. Mauri, *Phys. Rev. Lett.* **2007**, *99*, 176802.

[105] S. Pisana, M. Lazzeri, C. Casiraghi, K. S. Novoselov, A. K. Geim, A. C. Ferrari, F. Mauri, *Nat. Mater.* **2007**, *6*, 198.

[106] R. Beams, L. Gustavo Cançado, L. Novotny, *J. Phys.-Condes. Matter.* **2015**, *27*, 083002.

[107] J.-U. Lee, S. Woo, J. Park, H. C. Park, Y.-W. Son, H. Cheong, *Nat. Commun.* **2017**, *8*, 1370.

[108] T. M. G. Mohiuddin, A. Lombardo, R. R. Nair, A. Bonetti, G. Savini, R. Jalil, N. Bonini, D. M. Basko, C. Galiotis, N. Marzari, K. S. Novoselov, A. K. Geim, A. C. Ferrari, *Phys. Rev. B* **2009**, *79*, 8.

[109] T. Lin, X. Cong, M.-L. Lin, X.-L. Liu, P.-H. Tan, *Nanoscale* **2018**, *10*, 8704.

[110] W. Shi, X. Zhang, X.-L. Li, X.-F. Qiao, J.-B. Wu, J. Zhang, P.-H. Tan, *Chin. Phys. Lett.* **2016**, *33*, 057801.

[111] W. Shi, M. L. Lin, Q. H. Tan, X. F. Qiao, J. Zhang, P. H. Tan, *2D Mater.* **2016**, *3*, 025016.

[112] A. Merlen, J. G. Buijnsters, C. Pardanaud, *Coatings* **2017**, *7*, 55.

[113] T. Ando, *J. Phys. Soc. Jpn.* **2007**, *76*, 024712.

[114] M. O. Goerbig, J.-N. Fuchs, K. Kechedzhi, V. I. Fal'ko, *Phys. Rev. Lett.* **2007**, *99*, 4.

[115] J.-B. Wu, M.-L. Lin, X. Cong, H.-N. Liu, P.-H. Tan, *Chem. Soc. Rev.* **2018**, *47*, 1822.

[116] A. C. Ferrari, D. M. Basko, *Nat. Nanotechnol.* **2013**, *8*, 235.

[117] C. Jin, J. Kim, J. Suh, Z. Shi, B. Chen, X. Fan, M. Kam, K. Watanabe, T. Taniguchi, S. Tongay, A. Zettl, J. Wu, F. Wang, *Nat. Phys.* **2017**, *13*, 127.

[118] X. Cong, Q.-Q. Li, X. Zhang, M.-L. Lin, J.-B. Wu, X.-L. Liu, P. Venezuela, P.-H. Tan, *Carbon* **2019**, *149*, 19.

[119] X. Cong, J.-B. Wu, M.-L. Lin, W. Shi, P. Venezuela, P.-H. Tan, *Nanoscale* **2018**, *10*, 16138.

[120] M. L. Lin, Q. H. Tan, J. B. Wu, X. S. Chen, J. H. Wang, Y. H. Pan, X. Zhang, X. Cong, J. Zhang, W. Ji, P. A. Hu, K. H. Liu, P. H. Tan, *ACS Nano* **2018**, *12*, 8770.

[121] J.-B. Wu, X. Zhang, M. Ijäs, W.-P. Han, X.-F. Qiao, X.-L. Li, D.-S. Jiang, A. C. Ferrari, P.-H. Tan, *Nat. Commun.* **2014**, *5*, 8.

[122] J.-B. Wu, Z.-X. Hu, X. Zhang, W.-P. Han, Y. Lu, W. Shi, X.-F. Qiao, M. Ijiäs, S. Milana, W. Ji, A. C. Ferrari, P.-H. Tan, *ACS Nano* **2015**, *9*, 7440.

[123] A. D. Oyedele, S. Yang, L. Liang, A. A. Puretzky, K. Wang, J. Zhang, P. Yu, P. R. Pudasaini, A. W. Ghosh, Z. Liu, C. M. Rouleau, B. G. Sumpter, M. F. Chisholm, W. Zhou, P. D. Rack, D. B. Geohegan, K. Xiao, *J. Am. Chem. Soc.* **2017**, *139*, 14090.

[124] D. A. Chenet, B. Aslan, P. Y. Huang, C. Fan, A. M. Van Der Zande, T. F. Heinz, J. C. Hone, *Nano Lett.* **2015**, *15*, 5667.

[125] D. Wolverson, S. Crampin, A. S. Kazemi, A. Ilie, S. J. Bending, *ACS Nano* **2014**, *8*, 11154.

[126] M. Kim, S. Han, J. H. Kim, J. U. Lee, Z. Lee, H. Cheong, *2D Mater.* **2016**, *3*, 034004.

[127] Y. Tao, S. Xie, T. Lu, C. Hu, H. Liu, H. Zhang, X. Cheng, M. Liu, Z. Qi, *J. Appl. Phys.* **2022**, *131*, 165901.

[128] J. Xia, D.-F. Li, J.-D. Zhou, P. Yu, J.-H. Lin, J.-L. Kuo, H.-B. Li, Z. Liu, J.-X. Yan, Z.-X. Shen, *Small* **2017**, *13*, 1701887.

Xun Zhao received his B.E. degree from the Nanjing Institute of Technology in 2021. He is currently pursuing an M.E. degree under the supervision of Prof. Jiaxu Yan at the School of Flexible Electronics (IAM), Nanjing Tech University. His research interests include the Synthesis and Characterization of 2D Transition Metal Dichalcogenides and their applications, optoelectronic properties of layered 2D van der Waals nanomaterials and their potential device applications.

Jiaxu Yan is currently a professor at the Changchun Institute of Optics, Fine Mechanics and Physics (CIOMP), Chinese Academy of Sciences (CAS). Prof. Yan has long been engaged in laser spectroscopy of nano-semiconductor materials, semiconductor computational physics, and nano-semiconductor devices. He has published more than 30 papers as the first/corresponding author in Nat. Phys., Nat. Commun., Phys. Rev. Lett., J. Am. Chem. Soc., Adv. Mater. etc. Prof. Yan has been awarded the High-level Talent Program of the Chinese Academy of Sciences, Changbai Mountain Leading Talent, etc.